Variability of Upstream Proton Cyclotron Wave Properties and Occurrence at Mars Observed by MAVEN

O. M. Romeo, N. Romanelli, J. R. Espley, C. Mazelle, G. A. Dibraccio, J. R. Gruesbeck, J. S. Halekas

AGU ADVANCING EARTH AND SPACE SCIENCE

JGR Space Physics

RESEARCH ARTICLE
10.1029/2020JA028616

Variability of Upstream Proton Cyclotron Wave Properties and Occurrence at Mars Observed by MAVEN

O. M. Romeo[1,2], N. Romanelli[1,3], J. R. Espley[1], C. Mazelle[4], G. A. DiBraccio[1], J. R. Gruesbeck[1], and J. S. Halekas[5]

[1]NASA Goddard Space Flight Center, Greenbelt, MD, USA, [2]CRESST II, University of Maryland, College Park, MD, USA, [3]CRESST II, University of Maryland, Baltimore County, Baltimore, MD, USA, [4]Institut de Recherche en Astrophysique et Planétologie, CNRS – University of Toulouse – UPS – CNES, Toulouse, France, [5]Department of Physics and Astronomy, University of Iowa, Iowa City, IA, USA

Key Points:

- We confirm an annual periodicity of proton cyclotron wave occurrence rate upstream from the Martian bow shock between October 2014 and February 2020
- We report a decrease in median wave amplitude for each consecutive Martian perihelion based on available sampling of the Martian upstream region
- PCWs occur more frequently near perihelion for low to intermediate interplanetary magnetic field cone angles, slower solar wind speeds and higher solar wind densities

Supporting Information:

- Supporting Information S1
- Figure S1
- Figure S2
- Figure S3

Correspondence to:
O. M. Romeo,
oromeo@umd.edu

Citation:
Romeo, O. M., Romanelli, N., Espley, J. R., Mazelle, C., DiBraccio, G. A., Gruesbeck, J. R., & Halekas, J. S. (2021). Variability of upstream proton cyclotron wave properties and occurrence at Mars observed by MAVEN. *Journal of Geophysical Research: Space Physics*, *126*, e2020JA028616. https://doi.org/10.1029/2020JA028616

Received 21 AUG 2020
Accepted 17 NOV 2020

Abstract The presence of plasma waves upstream from the Martian bow shock, with frequencies near the local proton cyclotron frequency in the spacecraft frame, constitutes, in principle, an indirect signature for the existence of planetary protons from the ionization of Martian exospheric hydrogen. In this study, we determine the "proton cyclotron wave" (PCW) occurrence rate between October 2014 and February 2020, based on Magnetometer and Solar Wind Ion Analyzer measurements from the Mars Atmosphere and Volatile EvolutioN mission. We characterize its dependence on several wave and solar wind (SW) properties, and solar longitude ranges. We confirm a previously reported long-term trend with more PCWs near perihelion, likely associated with changes in exospheric hydrogen density. Furthermore, we report for the first time a decrease in median PCW amplitude for each consecutive Martian perihelion. Such variability cannot be attributed to differences in the distribution of SW conditions. This trend could be associated with changes in solar inputs, foreshock effects, and asymmetries due to the SW convective electric field influencing newborn protons. In addition, we observe PCWs more frequently for low to intermediate interplanetary magnetic field (IMF) cone angles, slower SW speeds, and higher SW proton densities. The IMF cone angle preference likely results from the trade-off between associated linear wave growth rates, wave saturation energies, and pick-up proton densities. Moreover, the dependencies on SW speed and density indicate the importance of the characteristic SW transit timescale and the charge exchange process coupling SW protons with the hydrogen exosphere.

1. Introduction

The solar wind (SW) interacts directly with the atmosphere and ionosphere of several solar system bodies lacking a global intrinsic magnetic field. Such coupling has been observed for active comets, Venus, and Mars (e.g., Acuña et al., 1998; Mazelle & Neubauer, 1993; Tsurutani, 1991; T. L. Zhang et al., 2008). In the Martian environment, the ionosphere and the exosphere act as an obstacle to slow down the incoming supermagnetosonic SW, forming a bow shock with a stand-off distance of about 1.6 R_M (Martian radii) from the center of the planet (Mazelle et al., 2004). Given that the hydrogen (H) exosphere extends beyond this boundary, neutral particles are ionized in the upstream region of Mars. The resulting newborn planetary protons are picked up by the magnetized SW flow, contributing to the planet's atmospheric loss (Chaffin et al., 2015; Chaufray et al., 2008; Jakosky et al., 2015; Yamauchi et al., 2015). These ions are the result of charge exchange, photoionization, or electron impact processes that affect the Martian H exosphere (M. H. G. Zhang et al., 1993).

Initially, the newborn protons are approximately at rest with respect to Mars. Thus, seen from the SW reference frame, these ions have a mean velocity approximately equal to $-\boldsymbol{v_{SW}}$, where $\boldsymbol{v_{SW}}$ is the solar wind velocity. The particles drift along the interplanetary magnetic field (IMF) $\boldsymbol{B}$ with a parallel velocity component $v_{\parallel}^{i} = -v_{SW}\cos(\alpha)$, where $v_{SW} = |\boldsymbol{v_{SW}}|$ and α is the angle between $\boldsymbol{v_{SW}}$ and $\boldsymbol{B}$, defined as the IMF cone angle. Additionally, the planetary ions gyrate about the IMF, with a perpendicular velocity component $v_{\perp}^{i} = -v_{SW}\sin(\alpha)$ and gyrofrequency $\Omega_i = q_i|\boldsymbol{B}|/m_i$, where q_i and m_i denote the ion charge and mass, respectively. Under these conditions, the resulting proton velocity distribution, consisting of a SW core and newborn ions, is most often highly unstable, capable of giving rise to several low frequency electromagnetic plasma wave modes (Brinca, 1991; Lee, 1989; Wu & Davidson, 1972; Wu & Hartle, 1974). In particular, the

interaction between planetary protons and the SW can excite the electromagnetic ion-ion right-hand (RH) and left-hand (LH) resonant instability modes depending, among other factors, on the IMF cone angle α.

The LH resonant instability has larger linear wave growth rates for large IMF cone angles and can be associated with related ring-beam or ring pick-up proton velocity distribution functions (Brinca & Tsurutani, 1989; Gary & Madland, 1988). In contrast, the RH resonant instability is, in many cases, the most easily excited mode for low to moderate IMF cone angles, associated with proton beam or ring-beam distributions (Gary, 1993). For both resonant instabilities, the observed wave frequency is Doppler-shifted due to the relative motion between the spacecraft (SC) and SW reference frames. As the spacecraft has a negligible planetocentric velocity compared to $\boldsymbol{v_{SW}}$, the observed wave frequency ω_{SC} in the SC reference frame is

$$\omega_{SC} = \omega - \boldsymbol{k} \cdot \boldsymbol{v}_{\parallel}^{\boldsymbol{SC}} \tag{1}$$

where ω is the wave frequency, $\boldsymbol{k}$ is the wave vector, and $\boldsymbol{v}_{\parallel}^{\boldsymbol{SC}} = -[\boldsymbol{v_{SW}} \cdot \hat{\boldsymbol{k}}]\,\hat{\boldsymbol{k}}$ is the spacecraft's velocity parallel to the wave propagation direction. Additionally, the expected wave frequency in the newborn ion reference frame is $\omega_i = \omega - \boldsymbol{k} \cdot \boldsymbol{v}^{\boldsymbol{i}}$ for both the RH and LH modes, where $\boldsymbol{v}^{\boldsymbol{i}}$ is the velocity of the newborn ions in the SW reference frame.

In particular, the RH resonant mode satisfies the following cyclotron resonance condition for moderate IMF cone angles:

$$\omega - \boldsymbol{k} \cdot \boldsymbol{v}_{\parallel}^{\boldsymbol{i}} + n\Omega_i = 0, \quad n = 1,2,3,\ldots \tag{2}$$

where $\boldsymbol{v}_{\parallel}^{\boldsymbol{i}}$ is the ion drift velocity along the magnetic field (Gary, 1991) in the SW reference frame. Given that the planetary newborn particles are approximately at rest initially with respect to Mars, the observed wave frequency in the SC reference frame for the RH mode is

$$\omega_{\mathrm{SC}} = -n\Omega_i \tag{3}$$

Thus, the observed frequency ω_{SC} is expected to be near the newborn ion gyrofrequency for $n = 1$ (fundamental mode), with the opposite polarization from the SW reference frame. Since the observed frequency is very close to the local proton cyclotron frequency, these waves are known as "proton cyclotron waves" (PCWs). However, we note that the term PCW refers to one of the wave's main observed signatures, and does not correspond, most of the time, to the ion cyclotron wave mode. The detection of PCWs constitutes, in principle, an indirect signature of the presence of newborn planetary protons (Brinca, 1991).

It is worth noticing that the term corresponding to the Doppler shift in Equation 1 is relatively small for the LH resonant mode. Therefore, waves generated from the LH instability are also expected to be observed with frequencies very close to the local ion gyrofrequency and left-hand polarized in the SC frame. In contrast with the RH resonant mode, these waves are expected to be left-hand polarized in both the SW and SC reference frames.

PCWs have been observed around Mars by several planetary missions. Russell et al. (1990) analyzed the first observations of PCWs upstream from the Martian bow shock with the Phobos 2 spacecraft. Additional studies of upstream PCWs were performed with data from the Mars Global Surveyor (MGS) and Mars Atmosphere and Volatile EvolutioN (MAVEN) missions. These waves have been observed to have frequencies very close to the local proton gyrofrquency, left-handed elliptical polarization in the SC reference frame, propagation angles ($\theta_{kB} \sim 20°$) quasi-parallel to the mean IMF direction, and are approximately planar (e.g., Bertucci et al., 2013; Brain et al., 2002; Liu et al., 2020; Mazelle et al., 2004; Romanelli et al., 2013, 2016; Wei & Russell, 2006; Wei et al., 2011, 2014). Among these works, Romanelli et al. (2013) reported the presence of a strong variability in the PCW occurrence rate between two different premapping subphases of the MGS mission. In particular, these changes were not found to be associated with MGS spatial biases or measured IMF cone angle distributions, suggesting that the observed variability in the occurrence rate could be related to temporal changes in properties of the Martian H exosphere.

Bertucci et al. (2013) then expanded upon this work, analyzing all premapping orbits of MGS from September 1997 to September 1998 for altitudes below 20,400 km (6 R_M). PCWs were found more frequently

near Martian perihelion and southern summer solstice, with a ~70% increase in average PCW occurrence rate compared to observations during periods close to the southern autumn and spring equinoxes. Bertucci et al. (2013) classified PCW events based on the identification of a clear spectral line in the power spectral density (PSD) of the transverse magnetic field component near the local proton cyclotron frequency f_c in the SC frame. However, the study did not take into account the polarization properties of the waves nor the PSD of the compressive component near f_c. These considerations would differentiate quasi-monochromatic wave events from dispersive wave packets generated by steepening of low frequency compressive nonlinear waves (Mazelle & Neubauer, 1993). Utilizing MAVEN observations, Romanelli et al. (2016) were able to apply more stringent criteria to identify PCWs, considering both frequency and polarization properties of the waves. Additionally, MAVEN observations upstream from the Martian bow shock allow broader spatial coverage over the planet, given that measurements are not constrained over the Martian south pole as was the case for MGS premapping orbits (Albee et al., 2001). Analyzing MAVEN data between October 2014 and March 2016 for about 1 Martian year, Romanelli et al. (2016) confirmed PCW abundance upstream from the Martian bow shock varies with time, with more waves detected near perihelion. Romanelli et al. (2016) also presented simulated exospheric H density profiles at higher altitudes that display a similar long-term trend, suggesting a coupling with the temporal variability of PCW occurrence rate.

Related studies have also reported changes in the Martian neutral and ionized environment on a similar timescale. Chaufray et al. (2015) simulated a 3D temporal model of the H exosphere and thermosphere to investigate the variability in exospheric H density and escape rate due to solar activity and Martian heliocentric distance. Yamauchi et al. (2015) analyzed Ion Mass Analyzer (IMA) data from the Mars Express (MEX) mission, and reported higher pick-up ion detection rates near perihelion for several Martian years, supporting a dependence between PCW occurrence and Martian heliocentric distance. Studies based on MAVEN measurements have shown exospheric H densities (Halekas, 2017; Rahmati et al., 2017) and escape rates (Rahmati et al., 2018) increase by an order of magnitude for time periods closer to perihelion compared to aphelion. Additionally, previous work has shown dust activity and water vapor concentrations high in the lower atmosphere to have an effect on the variability of the H exosphere (Bhattacharyya et al., 2015, 2017; Chaffin et al, 2014, 2017; Clarke et al, 2014, 2017; Fedorova et al, 2018, 2020; Heavens et al., 2018).

It is important to note that the MEX instrumental package does not include an onboard magnetometer, which prevents the direct detection of PCWs. In addition, MGS did not possess an onboard SW ion detection instrument to study SW properties during PCW events. As MAVEN provides both magnetic field and SW measurements, this mission presents an excellent opportunity to perform studies focused on these low frequency plasma waves (e.g., Andrés et al., 2020; Halekas et al., 2020; Liu et al., 2020). In this work, we present an extensive study with MAVEN observations covering almost 3 Martian years, identifying PCW events with strict criteria, to analyze the occurrence rate variability, main wave properties, and SW conditions that favor their presence. More specifically, we analyze measurements from the Magnetometer (MAG) and Solar Wind Ion Analyzer (SWIA) instruments on board the MAVEN spacecraft from October 2014 to February 2020.

This study is structured as follows. Section 2 provides information on the MAVEN mission, and the MAVEN MAG and SWIA instruments. A case study of an observed PCW event is also presented in this section. In Section 3, we describe the PCW selection criteria based on wave frequency and polarization properties. Section 4 reports the results on temporal variability of PCW abundance, main wave properties, and SW conditions favoring PCW generation. With data spanning almost 3 Martian years, MAVEN observations are grouped separately based on time intervals close to each Martian perihelion and aphelion to analyze wave and SW properties. In addition, the spatial coverage of MAVEN is provided in this section. Finally, the discussion and conclusions are presented in Sections 5 and 6, respectively.

2. MAVEN Observations of PCW Events Upstream from the Martian Bow Shock

2.1. MAVEN Mission and Instruments

The MAVEN spacecraft was launched in November 2013, arrived at Mars in September 2014, and is currently in its extended mission and relay phase. The orbit had a nominal periapsis altitude of 150 km, an apoapsis

altitude of 6,220 km, and a period of about 4.5 h (Jakosky et al., 2015). Currently, the periapsis altitude has been raised and apoapsis lowered to conserve fuel during the relay phase of the mission. The selected apoapsis altitude, orbital period, and orbital inclination (75°) allow orbital precession in both local time and latitude of the spacecraft periapsis, partially driven by the non-symmetric gravitational field. Additionally, the extent of the MAVEN apoapsis allows sampling of SW properties in many of its orbits.

The MAVEN MAG instrument is a dual-fluxgate magnetometer that provides vector magnetic field measurements over a broad range (to 65,536 nT per axis) with a sampling frequency of 32 Hz and accuracy of 0.25 nT (Connerney et al., 2015b). Upstream from the Martian bow shock, PCWs are characterized by a relatively low frequency (~0.06 Hz for an IMF intensity of ~4 nT) in the SC reference frame, compared to the MAG sampling cadence. Thus, in this work, we computed 4 Hz magnetic field averages from the 32 Hz MAG data, sufficient for the purposes of the present study. The MAVEN MAG field components are presented in the Mars-centered Solar Orbital (MSO) coordinate system, where the X axis is directed toward the Sun, the Z axis is perpendicular to Mars's orbital plane (positive toward the ecliptic north), and the Y axis completes the right-handed system.

Observations from SWIA on board MAVEN were also used to characterize SW conditions under which the waves are present. SWIA is an energy and angular ion spectrometer with electrostatic deflectors that measures ion fluxes over a broad energy range (25 eV/q – 25 keV/q) with a wide field of view of 360° × 90° (Halekas et al., 2015). In this analysis, we utilized the onboard-calculated moments of ion distribution functions for the SW velocity in MSO coordinates and SW density, with a temporal resolution of 4 s.

2.2. Case Study: PCW Event on November 26, 2018

Figure 1 presents an example of a PCW event observed by MAVEN MAG and SWIA upstream from the Martian bow shock on November 26, 2018, between 16:12:18 UT and 16:20:50 UT. Figures 1a–1d display the magnetic field and SW velocity MSO components and magnitude. Clear oscillations with a distinct frequency are observed for all magnetic field components during this time interval with a wave amplitude around 0.3 nT and a mean IMF of $\boldsymbol{B_0} = [2.6, -2.4, 0.9]$ nT. For this event, the mean SW velocity is $\boldsymbol{v_{SW}} = [-344.0, 54.7, 3.6]$ km s^{-1} and the IMF cone angle is $\alpha = 36.0°$, computed from MAG and SWIA measurements. Fluctuations in the SW velocity measurements have a similar frequency to the magnetic field oscillations. Figure 1e shows the ion density derived from SWIA, with a mean density of $n_{SW} = 4.3$ cm^{-3}. We find that these waves present a small degree of compressibility with $\sigma_{n_{SW}} / n_{SW} = 0.04$, where $\sigma_{n_{SW}}$ is the standard deviation of the density measurements during this time interval.

Figure 2a shows the PSD of the transverse $B_\perp$ and compressive $B_\parallel$ magnetic field components with respect to $\boldsymbol{B_0}$ for the same 512 s time interval in Figure 1. We implement a Hanning window to reduce spectral leakage and ensure a narrow main lobe. The associated local proton cyclotron frequency f_c for $B_0 = 3.7$ nT is 0.056 Hz, denoted by the vertical black line in Figure 2a. The value of $PSD[B_\perp]$ is maximized near f_c at a frequency of 0.051 Hz (0.91 f_c) and is larger than $PSD[B_\parallel]$ at the same frequency by a factor of ~28.

To determine the polarization and direction of propagation for the detected waves, we apply Minimum Variance Analysis (MVA) for subintervals corresponding to three local proton cyclotron gyroperiods within the 512 s interval (Sonnerup & Scheible, 1998). That is, we require at least three wave periods to identify and characterize waves with MVA. This technique consists of calculating the eigenvalues λ_j and eigenvectors $\boldsymbol{e_j}$ of the covariance matrix for the magnetic field MSO components in each subinterval. The maximum (λ_1), intermediate (λ_2), and minimum (λ_3) eigenvalues can be used to characterize properties of the detected waves. In particular, $\lambda_1/\lambda_2 \sim 1$ and $\lambda_2/\lambda_3 >> 1$ suggest a detection of circularly polarized and planar waves, respectively. When the assumption of planar waves is supported by the λ_2/λ_3 ratio, the direction of the wave vector $\boldsymbol{k}$ can also be approximated by the eigenvector $\boldsymbol{e_3}$ associated with the smallest eigenvalue. However, the eigenvector $\boldsymbol{e_3}$ only defines the direction of $\boldsymbol{k}$ and not the sense (Sonnerup & Scheible, 1998). We also apply Equations (3.3b, 3.4b, 3.8a) reported in Song and Russell (1999) to determine the wave amplitude δB, described as $\delta B = \sqrt{\lambda_1 - \lambda_3}$.

Figure 2b displays the magnetic field oscillations in the maximum-intermediate plane (hodogram) in the MVA basis ($\boldsymbol{e_1}$, $\boldsymbol{e_2}$, $\boldsymbol{e_3}$) for the subinterval 16:14:50–16:15:44 UT on November 26, 2018. The mean magnetic

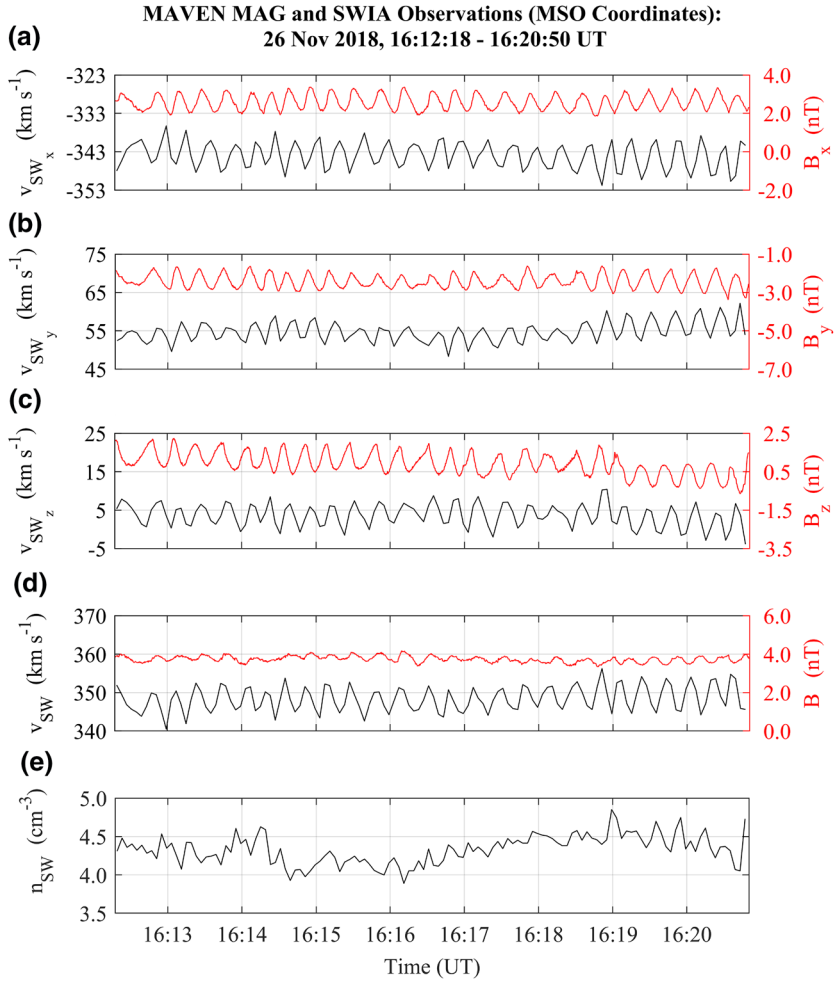

Figure 1. PCW event upstream from the Martian bow shock observed by the MAVEN MAG and SWIA instruments on November 26, 2018, 16:12:18–16:20:50 UT. (a)–(d) The magnetic field (red) and SW velocity (black) components and magnitude in MSO coordinates. (e) The SW ion density. MAG, Magnetometer; MAVEN, Mars Atmosphere and Volatile EvolutioN; MSO, Mars-centered Solar Orbital; SW, solar wind; SWIA, solar wind ion analyzer.

field in the MVA basis is $\boldsymbol{B}_0^{MVA} = [-0.5, -0.7, 3.7]$ nT, directed inwards toward the maximum-intermediate plane. The propagation angle θ_{kB} can be estimated by the angle between $\boldsymbol{e_3}$ and $\boldsymbol{B_0}$. We find that θ_{kB} is 16.0°, suggesting that these waves propagate quasi-parallel to the mean magnetic field upstream from the Martian bow shock. This wave event near the local proton cyclotron frequency is approximately circular ($\lambda_1/\lambda_2 = 1.07$) and planar ($\lambda_2/\lambda_3 = 82.52$), with a wave amplitude of $\delta B = 0.5$ nT. Based on the mean rotational direction of the magnetic field oscillations with respect to $\boldsymbol{B}_0^{MVA}$ (shown by the black arrow in Figure 2b), the wave is found to be left-hand polarized in the SC reference frame. All these results are consistent with previously reported properties of waves very close to the local proton cyclotron frequency upstream from Mars (Connerney et al., 2015a; Bertucci et al., 2013; Brain et al., 2002; Liu et al., 2020; Mazelle et al., 2004; Romanelli et al., 2013, 2016; Ruhunusiri et al., 2015, 2016; Russell et al., 1990; Wei & Russell, 2006; Wei et al., 2011, 2014).

3. PCW Selection Criteria

For this statistical study, we utilize a subset of MAVEN MAG and SWIA data from October 2014 to February 2020 representing 2.8 Martian years of observing time. To identify measurements in the upstream region of Mars, we consider the Martian bow shock fit from Gruesbeck et al. (2018) with an increased semilatus

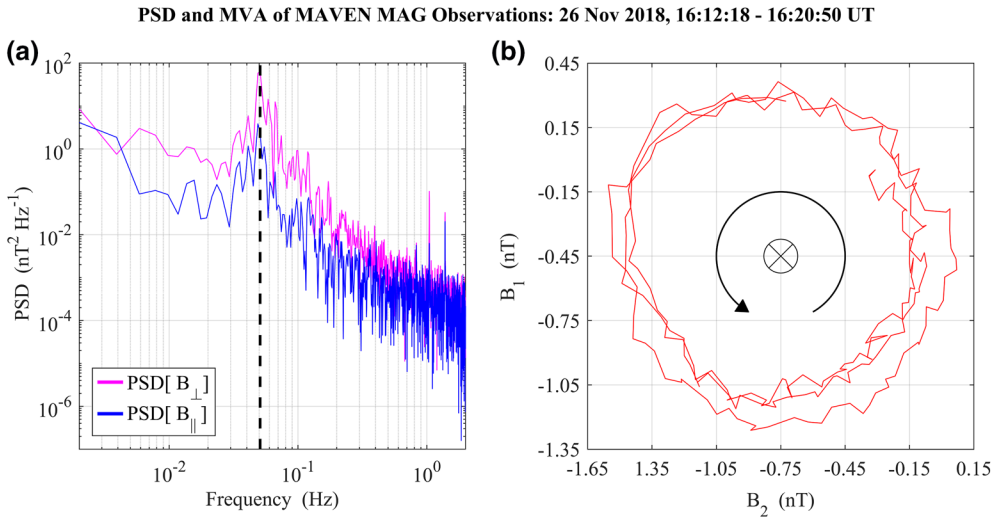

Figure 2. MAVEN MAG observations on November 26, 2018 16:12:18–16:20:50 UT for a PCW event. (a) Power spectral density (PSD) of the transverse (blue) and compressive (magenta) magnetic field components, where the dashed vertical line (black) indicates the mean local proton cyclotron frequency f_c. (b) Hodogram of the magnetic field observations in the maximum-intermediate MVA plane for the subinterval 16:14:50–16:15:44 UT, covering approximately three local proton cyclotron gyroperiods. The mean magnetic field is directed inwards toward the maximum-intermediate plane and the wave is left-hand polarized in the SC frame. MAG, Magnetometer; MAVEN, Mars Atmosphere and Volatile EvolutioN; MSO, Mars-centered Solar Orbital; PSD, power spectral density.

rectum corresponding to a 25% enlarged boundary. This extension of the fit accounts for variable bow shock expansions to ensure upstream wave detection near Mars. The upstream data from both instruments are then divided into 512 s time intervals with 90% overlap between contiguous segments. The length of this interval is sufficient to compute Fast Fourier transforms of PCW events, covering at least ~10 wave periods.

For each upstream 512 s interval, we consider a set of criteria to identify PCW events based on frequency and polarization properties of the waves. In order to combine the PSD and MVA techniques for the PCW selection criteria, the wave parameters derived from MVA for each ~3 gyroperiod subinterval are averaged over the 512 s interval. The first necessary condition for a PCW detection is based on the $PSD(f)$ of $B_\perp$, given by the expressions:

$$PSD[B_\perp]_{0.8f_c-\Delta f}^{1.2f_c+\Delta f} > \xi_\perp PSD[B_\perp]_{1.2f_c+\Delta f}^{1.4f_c+\Delta f} \tag{4a}$$

$$PSD\left[B_\perp\right]_{0.8f_c-\Delta f}^{1.2f_c+\Delta f} > \xi_\perp PSD\left[B_\perp\right]_{0.6f_c-\Delta f}^{0.8f_c-\Delta f} \tag{4b}$$

where the PSD is computed in a frequency interval centered around the local proton cyclotron frequency f_c, which must be greater by a factor $\xi_\perp$ compared to the PSD for two neighboring frequency intervals. The uncertainty Δf of f_c is associated with the MAG instrument's uncertainty ($\Delta B = 0.25$ nT) and is equal to 0.004 Hz. Once the peak in $PSD[B_\perp]$ is located at a frequency f close to the expected frequency f_c, the second criterion is

$$PSD[B_\perp]_f > \xi_\parallel PSD[B_\parallel]_f \tag{5}$$

through which we only consider cases with a peak in $PSD[B_\perp]$ larger than $PSD[B_\parallel]$ by a factor $\xi_\parallel$.

Based on the polarization properties obtained from MVA for each three cyclotron period subinterval, the third condition to identify PCWs is described by

$$\lambda_2 / \lambda_3 > \lambda_{23} \tag{6}$$

where the ratio of the eigenvalues for each subinterval is averaged over the 512 s interval and must be greater than the constant λ_{23}. Finally, we calculate the mean rotation vector of the magnetic field oscillations in

the $\boldsymbol{e_1} - \boldsymbol{e_2}$ plane for each subinterval from MVA. Detected waves are expected to have left-handed polarization in the SC frame, in which the e_3 – component of the mean rotational direction is anti-parallel to the e_3 – component of the mean magnetic field in the MVA basis. For each three gyroperiod subinterval s, we compute the scalar product between these two vectors and assign the resulting sign to the parameter p_s. Left-handed and right-handed polarization in each subinterval correspond to $p_s = -1$ and $p_s = 1$, respectively. p_s is then averaged over the entire 512 s interval from each subinterval to obtain the average polarization parameter p. Therefore, the fourth criterion to identify a PCW event is satisfied if $p < 0$, indicating that at least 50% of the subintervals are left-hand polarized within the 512 s interval.

To select the values of the constant terms associated with the selection criteria, we evaluated 36 different combinations of $\xi_\perp = \{1.0, 1.5, 2.0, 2.5, 3.0, 3.5\}$, $\xi_\parallel = \{1, 2, 3\}$ and $\lambda_{23} = \{5, 10\}$. Similar results for PCW temporal variability, main wave properties, and favorable SW conditions are observed for $\xi_\perp \geq 1.5$, $\xi_\parallel \geq 2$, and $\lambda_{23} \geq 5$. Therefore, to ensure reliable results with a sufficient number of total events, we set $\xi_\perp = 1.5$, $\xi_\parallel = 3$, and $\lambda_{23} = 5$ to identify PCWs in this statistical study.

4. Results

4.1. Temporal Variability of PCW Occurrence Rate Upstream from Mars

From October 2014 to February 2020, we find 529,652 time intervals in the upstream region with available data from both MAG and SWIA instruments. Figure 3a displays a histogram with the number of upstream 512 s intervals as a function of time with bin sizes of 15 terrestrial days. The lack of data in empty bins implies that either MAVEN was not upstream from the Martian bow shock or the instruments were not active. One 15 days bin (November–December 2019) is not considered to determine PCW abundance as it contains a relatively small number of upstream events (78 intervals). All other bins have at least 1,000 intervals, with an average of about 8,000 upstream events per bin. The bins with the lowest (November 2014) and highest (January–February 2019) number of upstream intervals contain 1,160 and 13,184 events, respectively.

Based on the selection criteria discussed in Section 3, we identify 50,730 PCW events. We compute the ratio of PCW events to the total number of upstream intervals for each 15 days bin to obtain the PCW occurrence rate as a function of time, shown in Figure 3b. The dashed black line emphasizes time intervals lacking observations upstream from Mars. The occurrence rate of PCWs near each Martian perihelion (PH) and northern winter solstice (NWS) exhibit an increase up to 30–35%, significantly larger than the average PCW occurrence rate of ∼2% close to aphelion (AH) for each Martian year. Near Martian aphelion, the PCW occurrence rate remains approximately constant below ∼3%. Each of the three main peaks occurs within a Martian solar longitude (L_s) range of $L_s = 280$–$302°$, slightly after PH ($L_s = 251°$) and NWS ($L_s = 270°$). At the same time, the main increase in PCW occurrence rate for each year develops during part of the Martian dust storm season ($L_s = 180$–$360°$), denoted by the gray regions in Figure 3b. To analyze changes in PCW occurrence, wave properties and SW conditions based on the Martian heliocentric distance, we group the data into two different sets of time periods near PH and AH, considering the solar longitude and PCW occurrence rate. MAVEN data measured within the range $L_s = 215$–$315°$ are organized into three groups with high rates (HR) of PCW occurrence for each of the 3 Martian years (HR1, HR2, and HR3) close to PH. Upstream observations within the range $L_s = 35$–$135°$ are organized into three groups with low rates (LR) of PCW occurrence for each of the 3 Martian years (LR1, LR2, and LR3) close to AH. Additionally, to assess possible seasonal sampling biases, Figure 3c displays the PCW occurrence rate as a function of the Martian solar longitude for the 3 Martian years analyzed. We have defined each Martian year to begin and end at $L_s = 175°$ based on the L_s ranges for the HR and LR groups, where the orange, green, and purple points correspond to the first (Y1), second (Y2), and third (Y3) Martian years.

We determined the HR solar longitude range based on PCW occurrence rates greater than 3%, which is above the maximum rate near each AH. Furthermore, the duration of the main increase in PCW abundance near PH is slightly different for each of the 3 Martian years. Therefore, we set the L_s range for the HR groups to cover all three time spans with high PCW occurrence rate. The LR solar longitude range is then defined by subtracting 180° from the HR range. Therefore, the corresponding time periods for the HR1, HR2, and HR3 groups are October 15, 2014–March 26, 2015, September 1, 2016–February 10, 2017, and July 20, 2018–December 29, 2018, respectively. The time periods for the LR1, LR2, and LR3 groups are August 31,

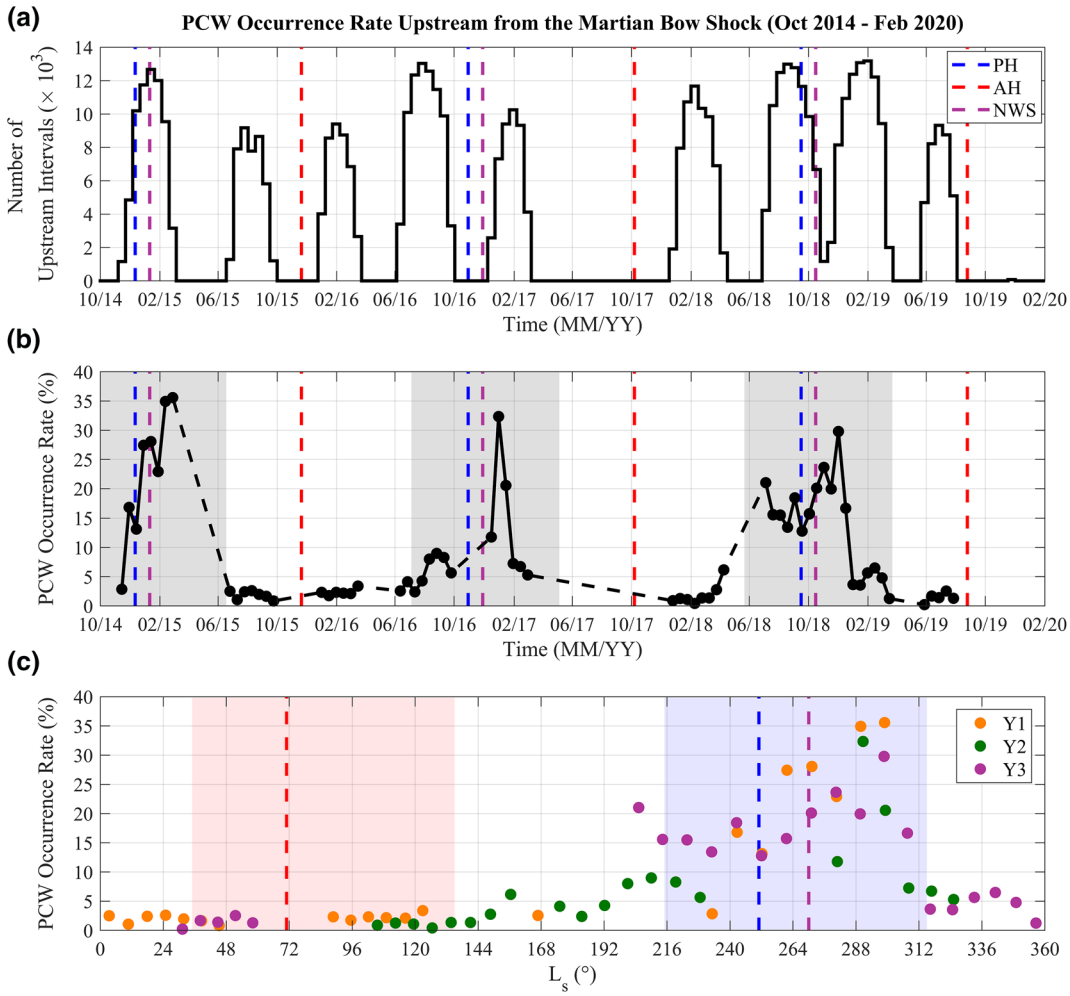

Figure 3. (a) Histogram of the number of 512 s time intervals (in thousands) upstream from the Martian bow shock from October 2014 to February 2020. The blue, purple, and red vertical dashed lines represent Martian perihelion (PH, $L_s = 251°$), northern winter solstice (NWS, $L_s = 270°$), and aphelion (AH, $L_s = 71°$), respectively. (b) PCW occurrence rate (%) as a function of time (black). The dashed black line indicates periods of upstream data gaps observed by MAVEN, and the gray regions correspond to periods of dust storm seasonal activity ($L_s = 180–360°$) for each Martian year. (c) PCW occurrence rate (%) as a function of solar longitude, with the orange, green and purple points corresponding to the first (Y1), second (Y2), and third (Y3) Martian years. The red and blue shaded regions represent the solar longitude range for the LR ($L_s = [35°, 135°]$) and HR ($L_s = [215°, 315°]$) groups, respectively. MAVEN, Mars Atmosphere and Volatile EvolutioN; PCW, proton cyclotron wave.

2015–April 9, 2016, July 18, 2017–February 25, 2018, and June 5, 2019–January 13, 2020, respectively. PCW occurrence rates for the HR1, HR2, and HR3 groups are 25% (65,321 upstream intervals), 14% (46,176 upstream intervals), and 16% (99,898 upstream intervals), respectively. Occurrence rates for the LR1, LR2, and LR3 groups are 2% (47,758 upstream intervals), 1% (40,045 upstream intervals), and 2% (31,473 upstream intervals), respectively.

As the MAVEN orbit around Mars varies with time, it is important to consider potential effects associated with seasonal sampling when comparing observations at approximately the same Martian longitude range. For instance, a larger number of intervals upstream from Mars are available for analysis around perihelion and NWS for HR1, compared to HR3. Moreover, the number of upstream intervals increases right after NWS for HR2. These differences may affect the observed shape and timing of the PCW occurrence peak in Figure 3b for each Martian year, when the number of upstream intervals is relatively small. However, as shown in Figure 3c, the three overlapping Martian years display a clear gradual increase of PCW occurrence rate to a peak slightly after perihelion and NWS, with steady rates around ~2% close to aphelion.

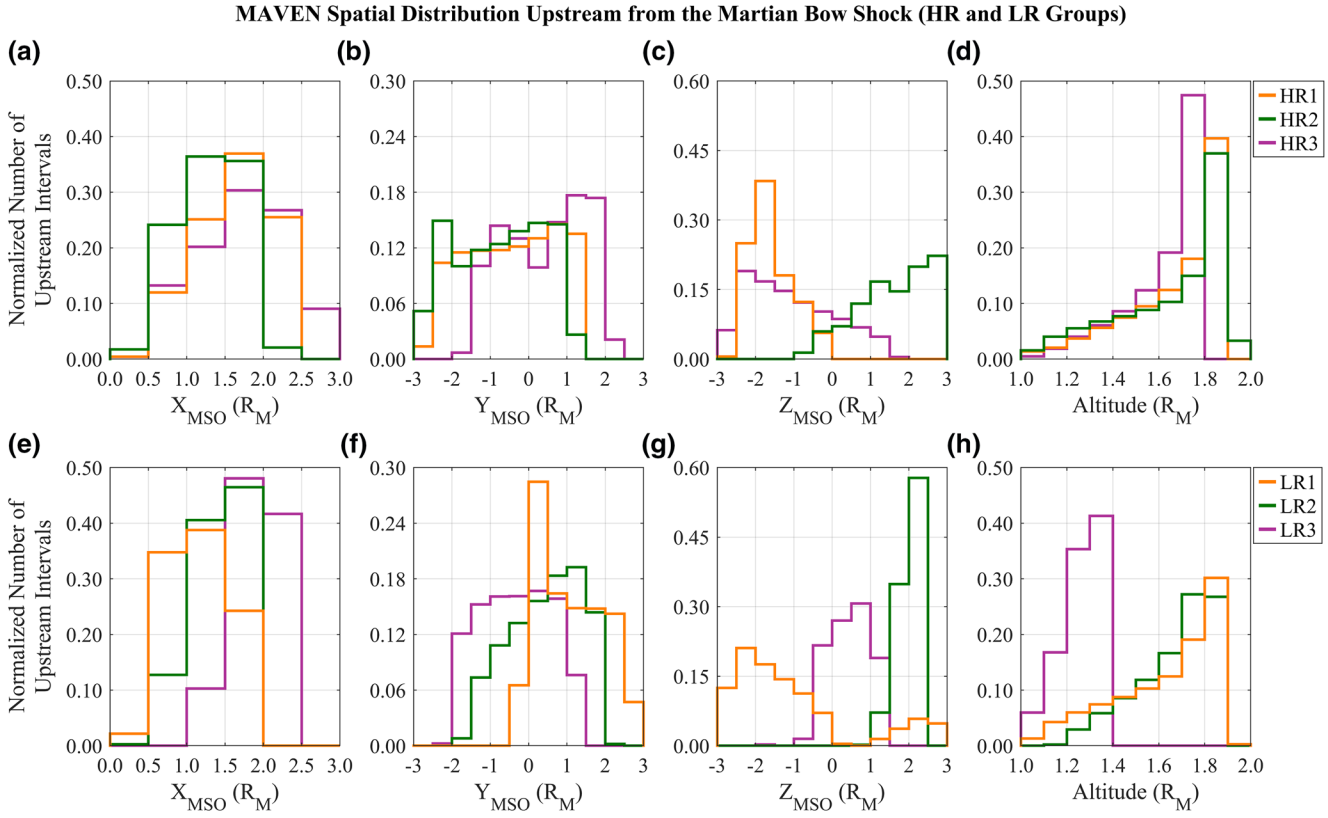

Figure 4. Normalized number of 512 s upstream intervals for HR1 (orange), HR2 (green), and HR3 (purple) as a function of (a) X_{MSO}, (b) Y_{MSO}, (c) Z_{MSO} and (d) altitude. Normalized Number of 512 s time intervals for LR1 (orange), LR2 (green), and LR3 (purple) as a function of (e) X_{MSO}, (f) Y_{MSO}, (g) Z_{MSO} and (h) altitude.

We also conduct an analysis of MAVEN spatial coverage in the upstream region to determine if the differences in PCW occurrence rate between the HR and LR groups could be associated with spacecraft sampling biases. We primarily focus on the SC X_{MSO}, Z_{MSO}, and altitude positions. Indeed, while the SW velocity is approximately along the X_{MSO} axis, defining the direction along which PCWs are convected, the Z_{MSO} coordinate sampling might introduce biases due to the asymmetric distribution of Martian crustal magnetic fields. We also consider spatial changes in the SC altitude over time as the most likely source of PCWs are ionized, exospheric H atoms whose density decays with the distance to Mars.

Figure 4 presents histograms of the normalized number of 512 s time intervals for the HR and LR groups as a function of each MSO spatial coordinate. The orbital coverage in the X_{MSO} direction mainly spans within the range 0.5–2.5 R_M, with orbits reaching up to 2.8 R_M for HR3. The distributions shown in Figures 4a and 4e for X_{MSO} are overall similar between the corresponding HR and LR groups. However, the LR1 histogram is slightly skewed toward lower X_{MSO} values compared to its HR counterpart. Most of the Y_{MSO} histograms cover a similar range between $-$ 3.0 R_M and 3.0 R_M, with the exception that the LR1 distribution is mainly sampled for positive Y_{MSO}. The most variable spatial coverage between the HR and LR groups is associated with the Z_{MSO} distributions, displayed in Figures 4c and 4g. The histogram for HR1 primarily samples the southern hemisphere, whereas both Martian hemispheres are covered by MAVEN for LR1. The HR2 histogram also primarily covers the southern hemisphere, while the northern hemisphere is sampled by MAVEN for LR2. Both HR and LR groups near the third Martian year mainly encompass the northern hemisphere. For the SC altitude shown in Figures 4d and 4h, most of the HR and LR histograms are very similar, between 1.0 R_M and 2.0 R_M, with the exception that the LR3 distribution samples primarily lower altitudes. Therefore, Figure 4 suggests that changes in PCW occurrence rate between perihelion and aphelion are not likely attributed to sampling biases in X_{MSO}, Y_{MSO}, and SC altitude as these spatial coordinates show small variability between the 3 Martian years.

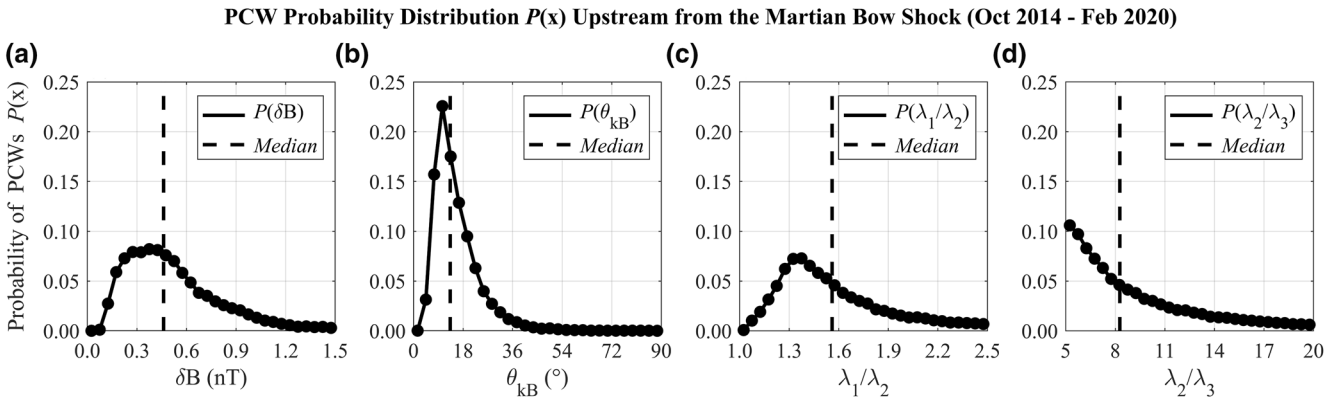

Figure 5. Probability distribution $P(x)$ of PCWs in the upstream region from October 2014 to February 2020 as a function of (a) δB, (b) θ_{kB}, (c) λ_1/λ_2 and (d) λ_2/λ_3. The dashed vertical line represents the median value in each probability distribution. PCW, proton cyclotron wave.

4.2. PCW Main Properties

In this section, we only consider upstream time intervals identified as PCW events according to the selection criteria given in Section 3. We define the PCW probability distribution function $P(x)$ by discretizing the number of PCW events into bins of a given wave property x and normalizing by the total number of PCW intervals. The integral of the function $P(x)$, bounded by the lower and upper limits of x, is equal to one, whereas this is not the case for the observed PCW occurrence rate. Figure 5 displays the PCW probability distribution $P(x)$ upstream from the Martian bow shock from October 2014 to February 2020 for various wave properties derived from MVA. The bin sizes for wave amplitude δB, propagation angle θ_{kB}, λ_1/λ_2, and λ_2/λ_3 are 0.05 nT, 3°, 0.05, and 0.50, respectively. The PCW probability distribution for wave amplitude is shown in Figure 5a, with a median amplitude of $\delta B = 0.46$ nT. $P(\delta B)$ reaches a maximum plateau for wave amplitudes $\delta B = 0.20$–0.55 nT. Figure 5b displays $P(\theta_{kB})$, with median and mode θ_{kB} values equal to 13.3° and 10.5°, respectively. The PCW probability distribution for λ_1/λ_2 is presented in Figure 5c, with median and mode λ_1/λ_2 values equal to 1.56 and 1.35, respectively. Finally, a decreasing trend in $P(\lambda_2/\lambda_3)$ is displayed in Figure 5d, with a median value of $\lambda_2/\lambda_3 = 8.28$.

Figure 6 presents the probability distribution function of PCWs, separated into the three HR and LR groups, for the same wave properties. The bin widths for each wave property are analogous to the sizes considered in Figure 5. The mode values of δB for the HR1, HR2, and HR3 probability distributions are 0.53 nT, 0.38 nT, and 0.23 nT, respectively. Indeed, we observe that the location of the peak in $P(\delta B)$ shifts to lower δB values for each consecutive Martian year near PH. Similarly, the median amplitude also decreases for each HR group, with median values of 0.65 nT, 0.52 nT, and 0.37 nT for HR1, HR2, and HR3, respectively. Moreover, we find a similar trend for the PCW probability distribution of normalized wave amplitude ($\delta B/B$), shown in Figure S1. Lower median amplitudes compared to HR are observed for the LR groups with δB around 0.35 nT. $P(\theta_{kB})$ is almost identical for all HR groups, with median and mode θ_{kB} values around 13.0° and 10.5°, respectively. More variation in the PCW probability distribution for θ_{kB} is found between the LR groups, with median θ_{kB} values closer to 21.0°. $P(\lambda_1/\lambda_2)$ tends to peak around 1.35 with a median λ_1/λ_2 value of about 1.55 for all HR groups, while the LR distributions are centered closer to one. Finally, median values of λ_2/λ_3 in each HR probability distribution are constantly higher than the corresponding LR group.

The observed variability of the PCW median amplitude between HR groups can be due to several factors. As a result, next we study the relationship between median amplitude and MAVEN position. Figures 7a and 7b show the median amplitude of PCWs for the three HR groups as a function of X_{MSO} and altitude with bin sizes of 0.5 R_M and 0.1 R_M, respectively. We consider bins with at least 100 events to compute the median PCW amplitude. All groups show a decreasing trend between the amplitude and the X_{MSO} coordinate. We also find that the median amplitudes of HR1 are greater than that of the other groups, whereas the smallest amplitudes are shown for HR3. Figure 7b also displays HR1 with larger median amplitudes than the other groups, while the smallest PCW amplitudes are found for HR3. Thus, Figure 7a would suggest that Mars is the source of these waves as the amplitude decreases with increasing distance from the planet, along the

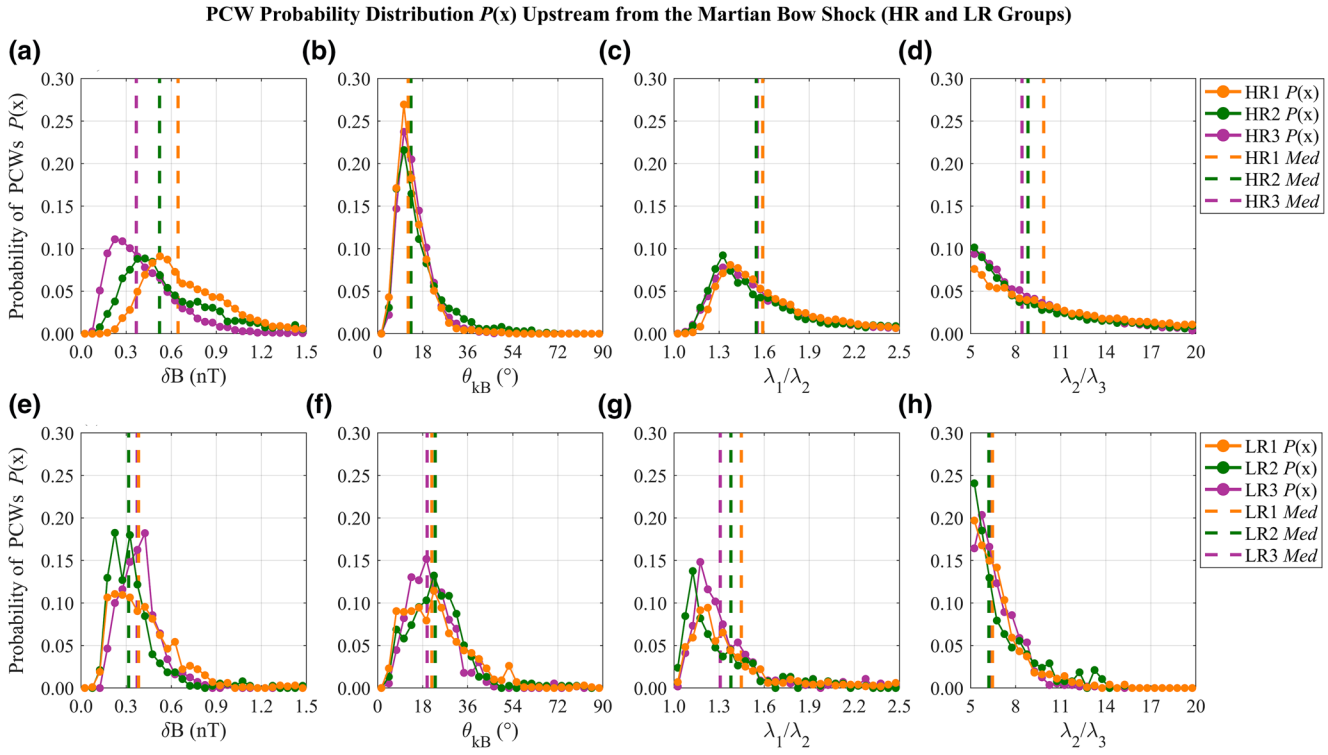

Figure 6. Probability distribution $P(x)$ of PCWs in the upstream region for HR1 (orange), HR2 (green), and HR3 (purple) as a function of (a) δB, (b) θ_{kB}, (c) λ_1/λ_2 and (d) λ_2/λ_3. For the LR1 (orange), LR2 (green), and LR3 (purple) groups, the probability distribution $P(x)$ of PCWs as a function of (e) δB, (f) θ_{kB}, (g) λ_1/λ_2, and (h) λ_2/λ_3. The dashed vertical line represents the median value in each probability distribution for HR and LR groups. PCW, proton cyclotron wave.

Mars-Sun axis. However, we do not find a similar monotonically decreasing trend between the median amplitude and altitude in all HR groups. This is also the case for analogous plots displaying the median wave amplitude as a function of the Y_{MSO} and Z_{MSO} coordinates, shown in Figure S2. It is worth mentioning

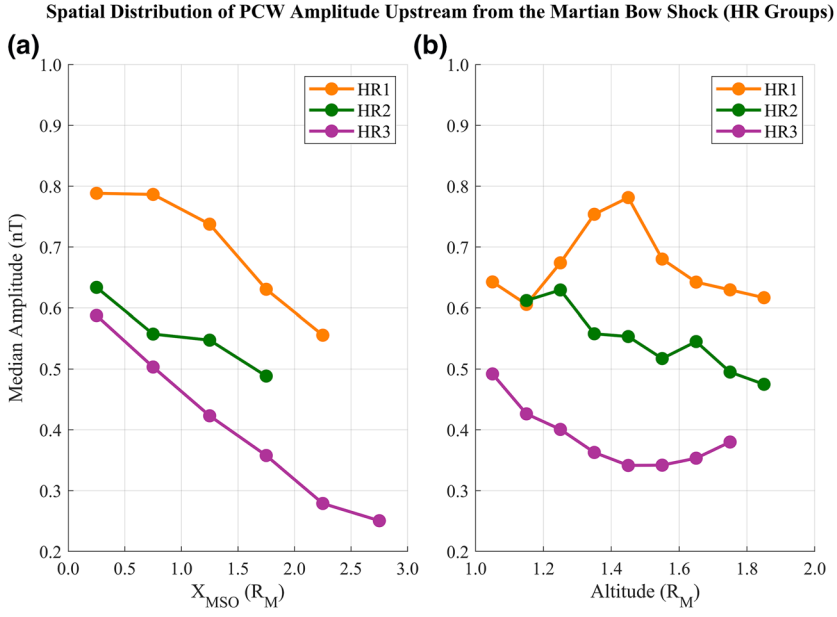

Figure 7. Median amplitude of upstream PCWs for the HR1 (orange), HR2 (green), and HR3 (purple) groups as a function of (a) X_{MSO} and (b) altitude.

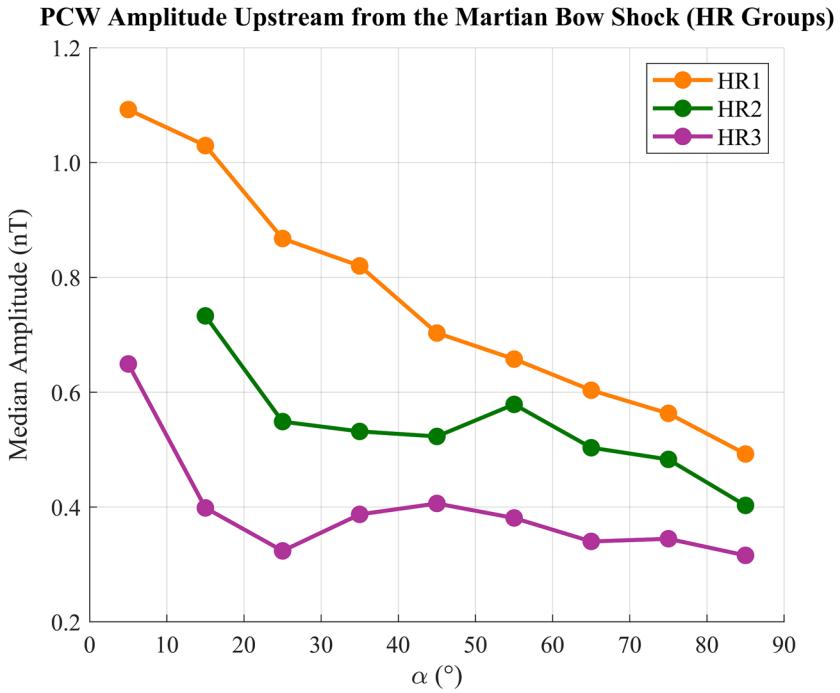

Figure 8. Median amplitude of PCWs in the upstream region for the HR1 (orange), HR2 (green), and HR3 (purple) groups as a function of IMF cone angle α. IMF, interplanetary magnetic field; PCW, proton cyclotron wave.

that the decreasing trend in median amplitude when comparing these three Martian perihelion periods is observed for measurements inside and outside the foreshock of Mars, and also for the normalized wave amplitude ($\delta B/B$).

In addition, we analyze the relationship between PCW amplitude and IMF cone angle for each HR group, shown in Figure 8. The median amplitude is calculated for α bin sizes of 10°, with a range from about 0.2 nT to 1.2 nT. Similar to Figure 7a, the HR1 curve has the largest amplitudes for all IMF cone angles, whereas the smallest median amplitudes are observed for HR3. A strong decreasing trend for median amplitude as a function of α is shown for HR1, while the magnitude of the slope, on average, decreases with each consecutive Martian year.

4.3. Solar Wind Conditions Favoring PCW Generation

Figures 9a–9e display histograms of the number of upstream 512 s time intervals as a function of IMF cone angle α, SW speed v_{SW}, Alfvén speed v_A, SW ion density n_{SW}, and SW proton flux $n_{SW}v_{SW}$, with bin sizes of 5°, 50 km s^{-1}, 10 km s^{-1}, 4.0 cm^{-3}, and 2.0×10^8 cm^2 s^{-1}, respectively. The Alfvén speed is computed with the SW proton density from SWIA, assuming the SW is composed of protons, and magnetic field measurements from the MAG instrument. Most of the upstream intervals are observed under $\alpha > 45°$, $v_{SW} \sim 350$ km s^{-1}, $v_A \sim 35$ km s^{-1}, $n_{SW} < 4$ cm^{-3}, and $n_{SW}v_{SW} \sim 10^8$ cm^2 s^{-1}. To compute the PCW occurrence rate, we consider bins with at least 100 upstream intervals for each histogram to ensure sufficient statistics.

Similar to Figure 3b, we calculate the PCW occurrence rate from the ratio of identified PCW events to the total number of upstream intervals within each bin for the SW parameters. As seen in Figure 9f, more PCWs occur for low to intermediate cone angles ($20° < \alpha < 45°$), with a distinct peak at 22.5°. A small peak between 50° and 60° is also apparent, very close to the Parker spiral angle of Mars (~55°). Figure 9g presents a decreasing trend in PCW occurrence rate of about 14% with increasing SW speed. The occurrence rate increases for larger Alfvén speeds until a value of about 75 km s^{-1}, as shown in Figure 9h. Figures 9i and 9j display a similar increasing trend in PCW abundance as a function of both SW proton density and flux, respectively.

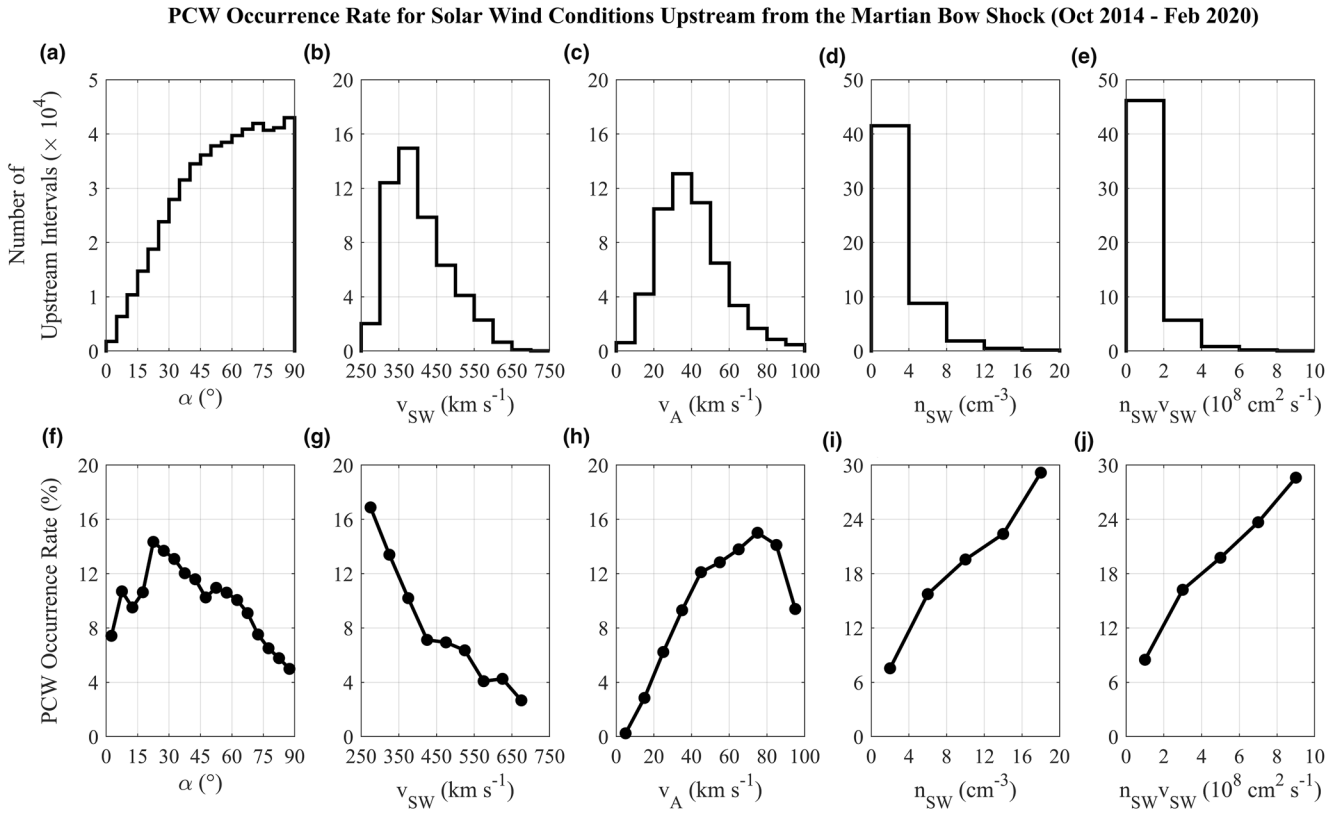

Figure 9. Histograms of the number of 512 s time intervals (in ten thousands) upstream from the Martian bow shock as a function of (a) IMF cone angle α, (b) SW speed v_{SW}, (c) Alfvén speed v_A, (d) SW density n_{SW} and (e) SW proton flux $n_{SW}v_{SW}$ between October 2014 and February 2020. PCW occurrence rate (%) as a function of (f) IMF cone angle α, (g) SW speed v_{SW}, (h) Alfvén speed v_A, (i) SW density n_{SW}, and (j) SW proton flux $n_{SW}v_{SW}$. IMF, interplanetary magnetic field; SW, solar wind.

Figure 10 presents the PCW occurrence rate for the same SW parameters displayed in Figure 9, for each HR group. The LR groups are not shown as the PCW occurrence rate for each bin is too low (<1%) to determine any significant trends with the SW conditions. Figures 10a–10e show the normalized number of upstream time intervals for each SW parameter. We find similar distributions for the IMF cone angle, SW proton density, and proton flux for all HR groups. The v_{SW} histogram for HR2 is centered at slightly faster speeds and the v_A histogram for HR3 is centered at slightly slower speeds compared to the remaining HR groups. In Figure 10f, the HR1 group shows more PCWs for $20° < \alpha < 45°$, with a large peak at $\alpha \sim 22.5°$. The PCW occurrence rate is maximized for IMF cone angles between 20° and 60° in the HR2 group. The occurrence rate for HR3 is approximately constant before dropping off around $\alpha = 60°$. The PCW abundance in Figure 10g decreases for faster SW speeds among all HR groups. In Figure 10h, PCW occurrence rate for the HR2 and HR3 curves increases for faster Alfvén speeds up to 75 km s^{-1}. However, we do not observe a similar trend in HR1 for $v_A > 25$ km s^{-1}. Figures 10i and 10j display an increasing trend in PCW abundance for both SW proton density and flux for all HR groups, respectively.

5. Discussion

We present a comprehensive study of PCWs utilizing both magnetic field and plasma observations from MAVEN, encompassing ~2.8 Martian years of data. This work expands upon the analysis of Romanelli et al. (2016) based on MAVEN MAG and extreme ultraviolet (EUV) measurements and numerical simulations, as well as the work by Romanelli et al. (2013) and Bertucci et al. (2013), based on MGS MAG data. These earlier studies suggested a long-term trend, on a timescale of about 1 Martian year, where PCWs are observed more frequently near Martian perihelion. In this work, we confirm the presence of such an annual trend, in which a gradual increase of about 30–35% in occurrence rate is found near perihelion and northern

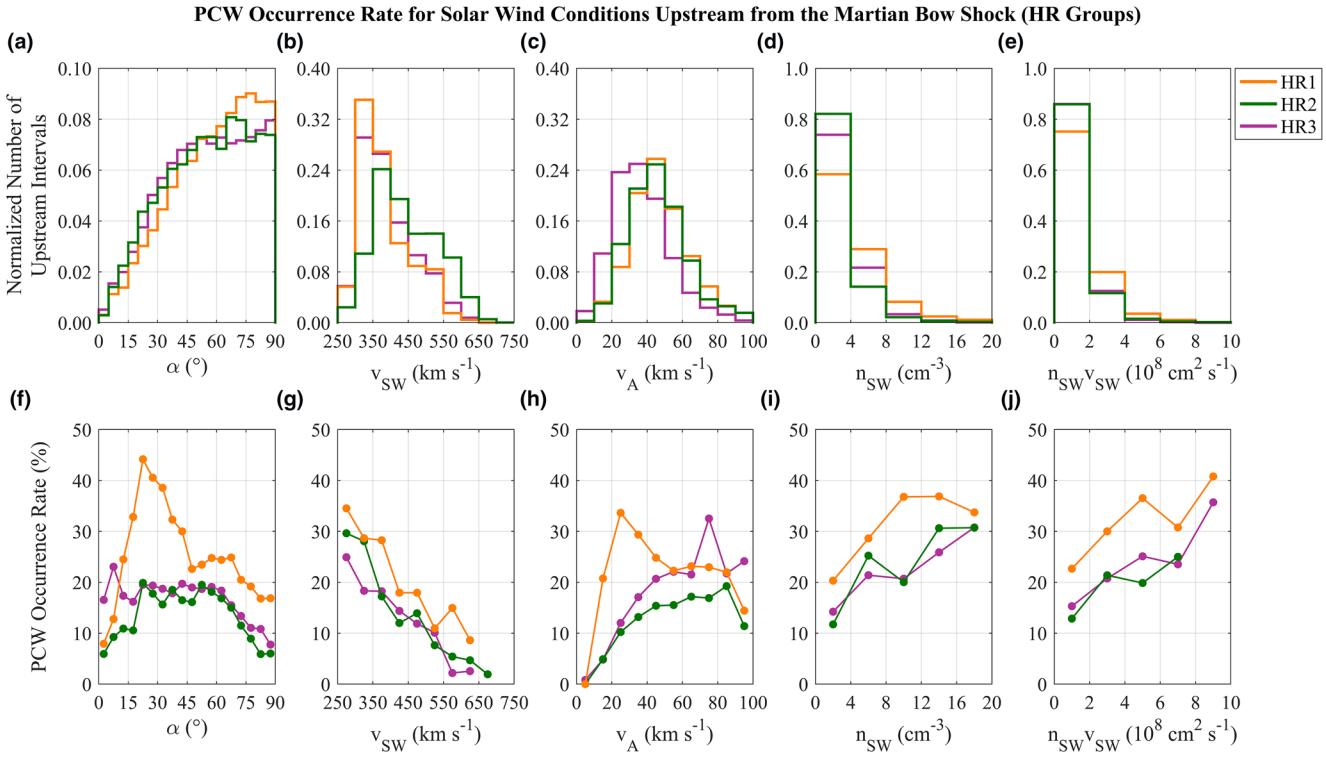

Figure 10. HR1 (orange), HR2 (green), and HR3 (purple) histograms of the normalized number of 512 s time intervals upstream from the Martian bow shock as a function of (a) IMF cone angle α, (b) SW speed v_{SW}, (c) Alfvén speed v_A, (d) SW density n_{SW} and (e) SW proton flux $n_{SW}v_{SW}$ between October 2014 and February 2020. PCW occurrence rate (%) for the HR1 (orange), HR2 (green), and HR3 (purple) groups as a function of (f) IMF cone angle α, (g) SW speed v_{SW}, (h) Alfvén speed v_A, (i) SW density n_{SW} and (j) SW proton flux $n_{SW}v_{SW}$. IMF, interplanetary magnetic field; SW, solar wind.

winter solstice for each Martian year. In contrast, rates of PCW occurrence remain below about 3% during time periods close to Martian aphelion, agreeing with previous results.

A similar long-term trend was reported for the temporal variability of exospheric H column density by Halekas (2017). Upstream H density is found to peak between solar longitudes of 263° and 288°, in which densities observed near perihelion are an order of magnitude larger compared to periods close to aphelion (Halekas, 2017). Slightly offset from this L_s range, the three peaks in PCW occurrence rate, shown in Figure 3b, occur between solar longitudes of 280° and 302°. This would indicate a time lag between Martian perihelion, peak exospheric H density, and peak PCW abundance. Halekas (2017) suggested the observed lag between perihelion and peak H density could be the result of delayed upper atmospheric responses to solar inputs, or seasonal effects in combination with direct solar EUV flux influence. In this regard, simulated profiles of upper exospheric H densities in the upstream region between 10,000 and 20,000 km have been found to be more directly linked to changes in temperature at the exobase, dependent on solar EUV fluxes (Chaufray et al., 2015; Romanelli et al., 2016). Daily irradiances observed by the MAVEN Extreme Ultraviolet Monitor (EUVM) instrument (Eparvier et al., 2015) also display a long-term temporal trend with increasing intensity for smaller heliocentric distance (e.g., Romanelli et al., 2016; Thiemann et al., 2017), similar to the timescale of exospheric H density variability. The ionization of more planetary particles under denser exospheric H profiles near perihelion could then increase the newborn ion population density, potentially providing more energy to increase the observed abundance of PCWs. Interestingly, we identify an average delay of ~25 days between the H density peak and PCW occurrence rate peak. We also report an asymmetry between the growth and decay phases of PCW abundance, as displayed in Figure 3b. Such features are found for the 3 Martian years near each perihelion explored in this work, consistent with previous observations (Romanelli et al., 2016). Possible causes for the observed time lag and asymmetry are not currently understood, however such signatures could be partly related to the seasonal sampling biases close to perihelion and NWS that can be seen in Figures 3a and 3c.

Moreover, dust activity and atmospheric upwelling can have a significant role in varying lower atmospheric water vapor concentration, influencing H exosphere variability. This has been suggested by several studies, including work based on MAVEN, MEX, and Hubble Space Telescope scattered Lyman α brightness observations (e.g., Bhattacharyya et al., 2015, 2017, 2020; Chaffin et al., 2014; Clarke et al., 2014, 2017). Martian regional dust storms have been observed to increase the near-surface atmospheric temperature at 0.5 mbar by 15–20 K, whereas planet-encircling dust storms can raise the temperature by 30–40 K, due to an increased opacity of the lower atmosphere (Smith, 2009). This effect can amplify atmospheric large scale circulation, allowing water vapor near the Martian surface to freely mix up to higher thermospheric altitudes (Chaffin et al., 2014). Therefore, initial large concentrations of water vapor high in the lower atmosphere could affect the H exosphere (Aoki et al., 2019; Bhattacharyya et al., 2015; Chaffin et al., 2017; Clarke et al., 2014; Fedorova et al., 2006, 2009, 2018, 2020; Heavens et al., 2018; Maltagliati et al., 2011, 2013). For each Martian year, higher PCW occurrence rates take place during part of the dust storm season, shown by the gray regions in Figure 3b. In this regard, it is worth mentioning that we observe a smaller secondary peak (~20%) in the PCW occurrence rate between June and July 2018, 2–3 months before the third Martian perihelion. In contrast, we do not find a similar secondary peak greater than ~15% in occurrence rate a few months before perihelion for the other Martian years. The small peak of PCWs around July 2018 may be at least partly related to the global dust storm of summer 2018, the first global event since 2007 (Sánchez-Lavega et al., 2019). Global dust storms can occur from interactions between local and regional dust storms that extend the growth duration of dust lifting and create new sites of dust activity along the planet, distributing material almost completely around Mars within a timescale of 1–2 weeks (Smith & Guzewich, 2019). The 2018 dust event became a global scale storm by mid-June (L_s ~193°) and continued until early July (L_s ~205°) before dust activity declined to normal levels for the perihelion season in mid-September (L_s ~250°), occurring close to the time interval when the small peak in Figure 3b is observed (Guzewich et al., 2019). Additionally, we observe a small peak between January and March 2019 of about 7%, which could be linked to the early 2019 regional dust storm from L_s ~320–340° (Aoki et al., 2019; Fedorova et al., 2020).

It is important to note that this periodic trend in PCW occurrence as a function of time is present for various temporal bin sizes. Bin widths of 10–25 days with 1 day increments were tested to ensure that the trend observed in PCW occurrence rate is independent of bin size for weekly to monthly time scales. We selected 15 days to cover a sufficiently large temporal scale, similar to the time span of significant variations in observed planetary pick-up ion detection rate (Yamauchi et al., 2015). By displaying the PCW occurrence rate as a function of the Martian solar longitude (Figure 3c), we observe that the overall trend shows a gradual increase of PCW occurrence rate until a peak slightly after perihelion and NWS. While the HR1 group contains more observations closer to perihelion than HR3, suggesting that seasonal biases might affect comparisons between HR periods, it is also important to emphasize that Y3 still presents 1,000 upstream intervals or more in each bin during these times. Although the HR2 group does not have observations during perihelion or NWS, the shape and timing of the PCW occurrence rate peak is consistent with the long term trend observed for the other two periods. In addition, different values were considered for the constants $\xi_{\perp}$, $\xi_{\parallel}$, and λ_{23} in the selection criteria to identify variations in the occurrence rate. We find that PCW abundance is still maximized close to each perihelion in a Martian year for $\xi_{\perp} \geq 1.5$, $\xi_{\parallel} \geq 2$, and $\lambda_{23} \geq 5$, with smaller observed rates as these parameters are increased. Furthermore, we find that this annual trend cannot be associated with sampling biases based on the MSO spatial coverage of MAVEN. For example, we observe similar ranges of X_{MSO} for each Martian year between the HR and LR groups. MAVEN is also able to sample the northern and southern hemispheres during at least one HR and LR group throughout the 3 Martian years, suggesting the presence of the PCW occurrence rate peak is independent of the sampling of this coordinate. Since most of the HR and LR groups display similar distributions of SC altitude, and the altitude range covered by MAVEN is relatively small, our results indicate that the long-term trend cannot be associated from sampling biases in radial distance near Mars. We also find that this trend is still present when the analysis is restricted to measurements inside or outside of the Martian foreshock. Moreover, Romanelli et al. (2016) did not report the increase in PCW occurrence rate to be associated with variations in the angle between the SW and background magnetic field direction for the first Martian year. We confirm this result for the following 2 Martian years by comparing the IMF cone angle distributions for the HR and LR groups.

We also analyzed PCW wave properties as seen by MAVEN. We find that these waves have mainly moderate to large amplitudes (~0.1–1.0 nT), slightly larger than the range observed by Brain et al. (2002). More

PCWs in both HR and LR groups are observed in the θ_{kB} = 10–25° range, suggesting that these waves propagate quasi-parallel to $\boldsymbol{B}$, agreeing with results from Romanelli et al. (2013), without displaying a significant change with Martian heliocentric distance. The PCW distribution as a function of λ_1/λ_2 peaks at 1.35, indicating that these waves are primarily elliptical. The tail of $P(\lambda_1/\lambda_2)$ for relatively large λ_1/λ_2 values may be attributed to time intervals with solar wind discontinuities and not highly elliptical waves. However, we have checked that these events do not significantly affect the results presented in this study. Indeed, the number of events with $\lambda_1/\lambda_2 > 5$ account for less than 4% of the upstream intervals identified with PCWs. The LR distribution for PCW abundance is maximized at lower λ_1/λ_2 values compared to the corresponding HR groups. Thus, we find that these waves are closer to being circularly polarized for periods near Martian aphelion than perihelion. This difference could be associated with variations in the growth phase of waves at the observation time due, in turn, to changes in the linear wave growth rate as several SW and planetary properties vary between the HR and LR groups. Our study suggests that LR groups are characterized by low PCW occurrence rates, relatively low wave amplitudes and approximately circular polarization. Additionally, we report that PCWs in HR groups are closer to being planar than those observed in LR groups, based on the probability distributions as a function of λ_2/λ_3. Regardless of the group, we find that PCWs are left-hand polarized in the spacecraft frame.

In addition, we report PCW amplitude to decrease with distance along the X_{MSO} axis for all HR groups, shown in Figure 7a, suggesting that Mars is the source of these waves. This trend is consistent with the result reported by Halekas et al. (2020) based on MAVEN observations. In contrast, Figure 7b shows the HR amplitude curves do not necessarily decrease with larger altitudes from Mars. In agreement with our results, significant amplitude variations with altitude are not found with MAVEN data from October 2014 to November 2018 (Liu et al., 2020), whereas previous studies with MGS data have observed wave amplitudes to slowly decrease with radial distance from Mars (Brain et al., 2002; Romanelli et al., 2013; Wei & Russell, 2006; Wei et al., 2014). Such differences between results from the MAVEN and MGS missions may be attributed to different combinations of multiple SW and planetary properties influencing PCW amplitude during each Martian year, such as pick-up ion rates, pick-up velocity, pick-up geometry, and wave growth time (Wei et al., 2014). Moreover, it is worth emphasizing the difference in altitude range covered by MGS premapping orbits (up to ~15 R_M) and MAVEN's orbital trajectory. Future studies could analyze the relation between observed amplitude and radial distance from Mars based on these factors, combining spacecraft observations and numerical simulations.

Furthermore, we find a decrease in median and mode wave amplitudes by ~0.15 nT for each consecutive HR group. This result is not likely attributed to sampling biases in MSO spatial coverage, based on the relationship between wave amplitude and distance from the Martian bow shock. Each HR group covers a similar range in X_{MSO} and altitude. The decline of PCW amplitude for each Martian year is present for all measured X_{MSO} and altitude values within the spatial range of MAVEN. Analogous results are also found for the Y_{MSO} and Z_{MSO} coordinates, shown in Figure S2. Additionally, we do not observe significant differences in the distributions of SW conditions between HR groups, displayed in Figure 10a to 10e, that could be related to this trend. This analysis suggests the reduction in amplitude could be associated with foreshock biases (Mazelle et al., 2018; Meziane et al., 2017), asymmetries due to the SW convective electric field influencing newborn protons (Wei & Russell, 2006), or changes in the Martian atmospheric response to variability in several solar inputs and/or solar cycle effects. For instance, the photoionization frequency of exospheric H^+ near Mars can increase by a factor of 2, from solar minimum to solar maximum (Modolo et al., 2005).

A decreasing trend between the wave amplitude and IMF cone angle is also found for the HR1 group in this study. In contrast, we do not observe such strong decreasing trend for the HR2 and HR3 groups in Figure 8. Previous studies based on MGS and MAVEN measurements have observed an amplitude dependence on the IMF cone angle (Liu et al., 2020; Romanelli et al., 2013). This relationship has also been studied with numerical one-dimensional hybrid simulations of the Martian planetary environment by Cowee et al. (2012), indicating that saturation wave energy decreases for larger cone angles for an estimated ion production rate of $\Lambda = 3.4 \times 10^{-4}\ \mathrm{cm}^{-3}\ \mathrm{s}^{-1}$. However, Wei et al. (2014) did not find such dependence on α analyzing MGS MAG measurements from the first aerobraking phase of the mission, in agreement with our observations for the HR2 and HR3 groups. One possible explanation for this potential disagreement between the HR groups can be derived from the results by Cowee et al. (2012). As suggested in the study, PCWs observed upstream from

the Martian bow shock are not likely to be completely saturated. For instance, PCWs must travel at least for 10 cyclotron periods to reach wave saturation, assuming $\alpha = 0°$ (Cowee et al., 2012). If we consider a typical wave frequency of $f \sim 0.06$ Hz and SW velocity of $v_{SW} \sim 400$ km s^{-1}, the wave will be convected over a distance of $\sim 20\ R_M$ before achieving saturation. Therefore, PCWs with higher wave frequencies could reach saturation in shorter distances with respect to Mars. Indeed, if we restrict this analysis to wave frequencies greater than 0.07 Hz, we obtain similar frequency distributions for the HR groups, focusing on waves that are more likely to have reached saturation. After applying this constraint, we find all three curves to display a strong decreasing trend in amplitude with similar slopes, displayed in Figure S3. Consequently, our analysis suggests that variations in the measured wave frequency distributions between HR groups could be related to the different trends shown in Figure 8 for each Martian year, possibly explaining the disagreement between results reported in previous studies.

We have also analyzed the relationship between several SW conditions and the presence of these waves. The PCW occurrence rate as a function of IMF cone angle reveals that more waves are detected for low to intermediate cone angles ($20° < \alpha < 45°$), in agreement with Liu et al. (2020), Romanelli et al. (2013) and Wei et al. (2014). This is observed for HR1 and HR2, whereas high PCW abundance in HR3 occurs for a slightly larger range ($0° < \alpha < 60°$). The latter result for the HR3 distribution does not significantly change if we disregard MAVEN data from July 20, 2018 to September 15, 2018 (corresponding to the 2018 global dust storm duration) in our analysis. The peak near $\alpha = 22.5°$ in Figure 9f is mainly attributed from HR1, as can be seen from Figure 10f. This difference could be partly due to effects related to seasonal sampling biases near perihelion and NWS. For example, the value of the PCW occurrence rate peak in Figure 10f for HR1, and therefore in Figure 9f, can vary depending on the range of magnetic field intensity selected. For instance, we find better agreement between the distributions when the analysis is restricted to cases with $B \geq 4$ nT, where each Martian year displays a peak in PCW occurrence rate around $\alpha = 22.5°$. However, it is important to emphasize that despite of this variability, higher rates of PCW occurrence are consistently observed for IMF cone angles below 45°. As previously reported by Liu et al. (2020), an explanation for the preference for low to intermediate IMF cone angles could be the result of a trade-off between associated saturation wave energy, characteristic growth time and newborn planetary proton density. For instance, the ion-ion RH instability that is often the most easily excited mode for $\alpha < \sim 75°$ is characterized by relatively large saturation wave amplitudes and long growth times, but does not require high pick-up ion density when compared with the resonant plasma instability present at large IMF cone angles (Cowee et al., 2012; Liu et al., 2020). Therefore, the observed PCW occurrence rate peak for low to intermediate IMF cone angles could be the net result of different growth times and threshold planetary ion densities for the dominant plasma instability under a given IMF cone angle range.

PCWs are additionally observed for slower SW speeds ($v_{SW} < 400$ km s^{-1}), with a decreasing trend in occurrence rate for faster speeds. This is consistently seen for all HR groups and the entire span of available MAVEN data, confirming the results from Halekas et al. (2020) between September and November 2018. Although this trend disagrees with linear wave growth theory (Gary et al., 1986), Delva et al. (2015) also reported a similar case for PCWs near Venus from the Venus Express mission. Delva et al. (2015) associated this result with a larger transit time for newborn planetary protons to interact with the SW, contributing to the growing instability responsible for the presence of PCWs. This effect observed near Venus may also be the reason for increased PCW abundance during slower SW speed conditions near Mars. In addition, we do not find a significant relationship between PCW occurrence rate and Alfvén speed. Figure 9h displays a slight preference for 40 km s$^{-1} < v_A < 80$ km s^{-1}, however, Figure 10h shows a slightly opposite trend between HR1 and the other two HR groups. This discrepancy can be partly explained by seasonal sampling biases, which cause MAVEN to observe different PCW distributions of magnetic field intensity and SW density each Martian year, which directly affect Alfvén speed. Interestingly, as in the case for the PCW occurrence rate as a function of the IMF cone angle, when restricting the analysis to cases with $B \geq 4$ nT we observe an overall decreasing trend in occurrence rate for faster Alfvén speeds greater than 40 km s^{-1} for all Martian years, similar to the HR1 curve in Figure 10h. Thus, this analysis suggests that the identified discrepancy could be partly attributed to sampling biases in the magnetic field intensity due, in turn, to MAVEN sampling of the upstream region during each Martian year. A deeper study of this dependence is beyond the scope of this study.

As shown in Figure 10i, we find higher PCW occurrence rates for larger SW proton densities for all HR groups. Thus, this trend also confirms the result initially reported by Halekas et al. (2020). This relationship

does not seem to be in agreement with linear theory for most of the cases associated with the RH instability in the cool beam regime. Indeed, in these cases, the linear wave growth rate is expected to be proportional to the ratio of planetary ion density to the SW particle density (n_i/n_{SW}), therefore suggesting that more PCWs should be present for lower SW densities (Gary, 1991). However, an increase in the SW density gives rise to an increase in the charge exchange ionization frequency of the Martian H exosphere, which is linearly proportional to both SW speed and density (M. H. G. Zhang et al., 1993). Thus, despite the fact that higher SW densities reduce the expected linear wave growth rate, the same increase can give rise to higher newborn ion densities due to charge exchange, providing an explanation for the observed trend. In agreement with this interpretation, Rahmati et al. (2018) reported that charge exchange is the leading ionization mechanism of exospheric H atoms upstream from Mars, with a higher ionization frequency compared to that of photoionization and electron impact ionization processes.

Finally, our results allow us to provide estimates for the expected pitch angle range around which charged particles interacting with PCWs can be trapped near Mars, following the theoretical work by Mazelle et al. (2000, 2003), and Romanelli et al. (2018). $P(\delta B/B)$ is maximized for a normalized wave amplitude $\delta B/B$ ~0.1, shown in Figure S1. In addition, PCWs with this normalized amplitude are observed more frequently for an IMF cone angle range between $\alpha = 20°$ and the Parker spiral angle (~55°). As shown in Romanelli et al. (2018), these derived properties suggest PCWs that might arise from proton ring-beam distributions will tend to trap particles with approximately the same energy (in the wave rest frame) close to a pitch angle range between 40° and 60°. Future studies could test this prediction utilizing velocity distribution functions measured by SWIA.

6. Conclusions

This paper presents a statistical study with MAVEN magnetic field and plasma observations from October 2014 to February 2020 to analyze the temporal variability of PCW occurrence for about 3 Martian years. We confirm that PCWs tend to occur more frequently near each Martian perihelion and northern winter solstice. Our results suggest this long-term trend is associated with changes in the Martian heliocentric distance, likely due to variations in the H exosphere density and also possibly related to changes in water vapor concentrations in the lower and upper atmosphere influenced by dust activity. In particular, this variability does not seem to be related to biases in MAVEN spatial coverage, length of temporal binning, or the considered PCW selection criteria.

We also find that the observed PCWs propagate mostly quasi-parallel to the mean magnetic field direction, with amplitudes ranging from 0.1 nT to 1.0 nT, and are planar and elliptically left-hand polarized in the spacecraft reference frame. Our results suggest that the reduction in median amplitude between each Martian year cannot be attributed to the spatial coverage of each MSO coordinate nor differences in distributions of SW conditions. Such decrease could be associated with physical processes taking place in the Martian foreshock, the SW convective field influence on newborn protons, and/or temporal changes in solar inputs over these timescales. Finally, we observe these waves more frequently for low to intermediate IMF cone angles ($20° < \alpha < 45°$), slower SW speeds ($v_{SW} < 400$ km s^{-1}), and higher SW proton densities ($n_{SW} > 5$ cm^{-3}). As previously reported by Liu et al. (2020), the preference for this IMF cone angle range is likely the result of the trade-off between associated linear wave growth rates, wave saturation energies, and pick-up proton densities. Furthermore, while the PCW occurrence rate dependence on the SW speed seems to disagree with linear theory, this outcome could be associated with larger transit times for planetary pick-up protons to interact with the SW flow. In addition, the observed dependence on SW density suggests that an increase in the ionization frequency of H atoms by charge exchange is responsible for an increase in the newborn proton density, and therefore in the linear wave growth rate.

Future studies could be focused on the analysis of the observed temporal lag between Martian perihelion, peak exospheric H density, and peak PCW occurrence rate upstream from Mars. Such work would improve the current understanding on the relationship between exospheric H density and the generation of these upstream low frequency waves. In particular, confining the timescales of these phenomena, in addition to analyzing other related solar and planetary properties, could allow us to better understand the physical processes coupling the Martian atmosphere with the plasma environment.

Data Availability Statement

MAVEN data are publicly available through the Planetary Data System (https://pds-ppi.igpp.ucla.edu/index.jsp).

Acknowledgments
The MAVEN mission is supported by NASA through the Mars Scout program. O. M. Romeo is supported by CRESST II (Center for Research and Exploration in Space Sciences & Technology) and the University of Maryland, College Park. N. Romanelli is an Assistant Research Scientist at NASA Goddard Space Flight Center and the University of Maryland, Baltimore County hired through a cooperative agreement with CRESST II. The work by C. Mazelle is also supported by the French Space Agency CNES.

References

Acuña, M. H., Connerney, J. E. P., Wasilewski, P., Lin, R. P., Anderson, K. A., Carlson, C. W., et al. (1998). Magnetic field and plasma observations at Mars: Initial results of the Mars global surveyor mission. *Science*, *279*(5357), 1676–1680. https://doi.org/10.1126/science.279.5357.1676

Albee, A. L., Arvidson, R. E., Palluconi, F., & Thorpe, T. (2001). Overview of the Mars global surveyor mission. *Journal of Geophysical Research*, *106*(E10), 23291–23316. https://doi.org/10.1029/2000JE001306

Andrés, N., Romanelli, N., Hadid, L. Z., Sahraoui, F., DiBraccio, G., & Halekas, J. (2020). Solar wind turbulence around Mars: Relation between the energy cascade rate and the proton cyclotron waves activity. *The Astrophysical Journal*, *902*(2), 134. https://doi.org/10.3847/1538-4357/abb5a7

Aoki, S., Vandaele, A. C., Daerden, F., Villanueva, G. L., Liuzzi, G., Thomas, I. R., et al. (2019). Water vapor vertical profiles on Mars in dust storms observed by tgo/nomad. *Journal of Geophysical Research: Planets*, *124*(12), 3482–3497. https://doi.org/10.1029/2019JE006109

Bertucci, C., Romanelli, N., Chaufray, J.-Y., Gomez, D., Mazelle, C., Delva, M., et al. (2013). Temporal variability of waves at the proton cyclotron frequency upstream from Mars: Implications for Mars distant hydrogen exosphere. *Geophysical Research Letters*, *40*(15), 3809–3813. https://doi.org/10.1002/grl.50709

Bhattacharyya, D., Chaufray, J. Y., Mayyasi, M., Clarke, J. T., Stone, S., Yelle, R. V., et al. (2020). Two-dimensional model for the martian exosphere: Applications to hydrogen and deuterium Lyman α observations. *Icarus*, *339*, 113573. https://doi.org/10.1016/j.icarus.2019.113573

Bhattacharyya, D., Clarke, J. T., Bertaux, J.-L., Chaufray, J.-Y., & Mayyasi, M. (2015). A strong seasonal dependence in the martian hydrogen exosphere. *Geophysical Research Letters*, *42*(20), 8678–8685. https://doi.org/10.1002/2015GL065804

Bhattacharyya, D., Clarke, J. T., Chaufray, J.-Y., Mayyasi, M., Bertaux, J.-L., Chaffin, M. S., et al. (2017). Seasonal changes in hydrogen escape from Mars through analysis of hst observations of the martian exosphere near perihelion. *Journal of Geophysical Research: Space Physics*, *122*(11), 11756–11764. https://doi.org/10.1002/2017JA024572

Brain, D. A., Bagenal, F., Acuña, M. H., Connerney, J. E. P., Crider, D. H., Mazelle, C., et al. (2002). Observations of low-frequency electromagnetic plasma waves upstream from the martian shock. *Journal of Geophysical Research*, *107*(A6), 1076. https://doi.org/10.1029/2000JA000416

Brinca, A. (1991). Cometary linear instabilities: from profusion to perspective. In A. D. Johnstone (Ed.), Cometary plasma processes. (61, pp. 211–221). Washington, DC: American Geophysical Union (AGU). https://doi.org/10.1029/GM061p0211

Brinca, A., & Tsurutani, B. T. (1989). Influence of multiple ion species on low-frequency electromagnetic wave instabilities. *Journal of Geophysical Research*, *94*(A10), 13565–13569. https://doi.org/10.1029/JA094iA10p13565

Chaffin, M. S., Chaufray, J.-Y., Deighan, J., Schneider, N. M., McClintock, W. E., Stewart, A. I. F., et al. (2015). Three-dimensional structure in the Mars H corona revealed by IUVS on MAVEN. *Geophysical Research Letters*, *42*(21), 9001–9008. https://doi.org/10.1002/2015GL065287

Chaffin, M. S., Chaufray, J.-Y., Stewart, I., Montmessin, F., Schneider, N. M., & Bertaux, J.-L. (2014). Unexpected variability of martian hydrogen escape. *Geophysical Research Letters*, *41*(2), 314–320. https://doi.org/10.1002/2013GL058578

Chaffin, M. S., Deighan, J., Schneider, N. M., & Stewart, A. I. F. (2017). Elevated atmospheric escape of atomic hydrogen from Mars induced by high-altitude water. *Nature Geoscience*, *10*(3), 174–178. https://doi.org/10.1038/ngeo2887

Chaufray, J.-Y., Bertaux, J.-L., Leblanc, F., & Quémerais, E. (2008). Observation of the hydrogen corona with spicam on Mars express. *Icarus*, *195*(2), 598–613. https://doi.org/10.1016/j.icarus.2008.01.009

Chaufray, J.-Y., Gonzalez-Galindo, F., Forget, F., Lopez-Valverde, M. A., Leblanc, F., Modolo, R., et al. (2015). Variability of the hydrogen in the martian upper atmosphere as simulated by a 3d atmosphere–exosphere coupling. *Icarus*, *245*, 282–294. https://doi.org/10.1016/j.icarus.2014.08.038

Clarke, J. T., Bertaux, J.-L., Chaufray, J.-Y., Gladstone, G. R., Quémerais, E., Wilson, J. K., et al. (2014). A rapid decrease of the hydrogen corona of Mars. *Geophysical Research Letters*, *41*(22), 8013–8020. https://doi.org/10.1002/2014GL061803

Clarke, J. T., Mayyasi, M., Bhattacharyya, D., Schneider, N. M., Mcclintock, W. E., Deighan, J. I., et al. (2017). Variability of D and H in the Martian upper atmosphere observed with the MAVEN IUVS echelle channel. *Journal of Geophysical Research: Space Physics*, *122*(2), 2336–2344. https://doi.org/10.1002/2016JA023479

Connerney, J. E. P., Espley, J. R., DiBraccio, G. A., Gruesbeck, J. R., Oliversen, R. J., Mitchell, D. L., et al. (2015a). First results of the maven magnetic field investigation. *Geophysical Research Letters*, *42*(21), 8819–8827. https://doi.org/10.1002/2015GL065366

Connerney, J. E. P., Espley, J., Lawton, P., Murphy, S., Odom, J., Oliversen, R., et al. (2015b). The maven magnetic field investigation. *Space Science Reviews*, *195*(1–4), 257–291. https://doi.org/10.1007/s11214-015-0169-4

Cowee, M. M., Gary, S. P., & Wei, H. Y. (2012). Pickup ions and ion cyclotron wave amplitudes upstream of Mars: First results from the 1d hybrid simulation. *Geophysical Research Letters*, *39*(8), L08104. https://doi.org/10.1029/2012GL051313

Delva, M., Bertucci, C., Volwerk, M., Lundin, R., Mazelle, C., & Romanelli, N. (2015). Upstream proton cyclotron waves at Venus near solar maximum. *Journal of Geophysical Research: Space Physics*, *120*(1), 344–354. https://doi.org/10.1002/2014JA020318

Eparvier, F. G., Chamberlin, P. C., Woods, T. N., & Thiemann, E. M. B. (2015). The solar extreme ultraviolet monitor for MAVEN. *Space Science Reviews*, *195*(1–4), 293–301. https://doi.org/10.1007/s11214-015-0195-2

Fedorova, A. A., Bertaux, J.-L., Betsis, D., Montmessin, F., Korablev, O., Maltagliati, L., et al. (2018). Water vapor in the middle atmosphere of Mars during the 2007 global dust storm. *Icarus*, *300*, 440–457. https://doi.org/10.1016/j.icarus.2017.09.025

Fedorova, A. A., Korablev, O. I., Bertaux, J.-L., Rodin, A. V., Kiselev, A., & Perrier, S. (2006). Mars water vapor abundance from spicam ir spectrometer: Seasonal and geographic distributions. *Journal of Geophysical Research*, *111*(E9), E09S08. https://doi.org/10.1029/2006JE002695

Fedorova, A. A., Korablev, O. I., Bertaux, J.-L., Rodin, A. V., Montmessin, F., Belyaev, D. A., et al. (2009). Solar infrared occultation observations by SPICAM experiment on Mars-Express: Simultaneous measurements of the vertical distributions of H_2O, CO_2 and aerosol. *Icarus*, *200*(1), 96–117. https://doi.org/10.1016/j.icarus.2008.11.006

Fedorova, A. A., Montmessin, F., Korablev, O., Luginin, M., Trokhimovskiy, A., Belyaev, D. A., et al. (2020). Stormy water on Mars: The distribution and saturation of atmospheric water during the dusty season. *Science*, *367*(6475), 297–300. https://doi.org/10.1126/science.aay9522

Gary, S. P. (1991). Electromagnetic ion/ion instabilities and their consequences in space plasmas: A review. *Space Science Reviews*, *56*(3–4), 373–415. https://doi.org/10.1007/BF00196632

Gary, S. P. (1993). *Theory of space plasma microinstabilities (No. 7)*. Cambridge: Cambridge University Press. https://doi.org/10.1017/CBO9780511551512

Gary, S. P., & Madland, C. D. (1988). Electromagnetic ion instabilities in a cometary environment. *Journal of Geophysical Research*, *93*(A1), 235–241. https://doi.org/10.1029/JA093iA01p00235

Gary, S. P., Madland, C. D., Schriver, D., & Winske, D. (1986). Computer simulations of electromagnetic cool ion beam instabilities. *Journal of Geophysical Research*, *91*(A4), 4188–4200. https://doi.org/10.1029/JA091iA04p04188

Gruesbeck, J. R., Espley, J. R., Connerney, J. E. P., DiBraccio, G. A., Soobiah, Y. I., Brain, D., et al. (2018). The three-dimensional bow shock of Mars as observed by MAVEN. *Journal of Geophysical Research: Space Physics*, *123*(6), 4542–4555. https://doi.org/10.1029/2018JA025366

Guzewich, S. D., Lemmon, M., Smith, C. L., Martínez, G., de Vicente-Retortillo, Á., Newman, C. E., et al. (2019). Mars science laboratory observations of the 2018/Mars year 34 global dust storm. *Geophysical Research Letters*, *46*(1), 71–79. https://doi.org/10.1029/2018GL080839

Halekas, J. S. (2017). Seasonal variability of the hydrogen exosphere of Mars. *Journal of Geophysical Research: Planets*, *122*(5), 901–911. https://doi.org/10.1002/2017JE005306

Halekas, J. S., Ruhunusiri, S., Vaisberg, O. L., Harada, Y., Espley, J., Mitchell, D. L., et al. (2020). Properties of plasma waves observed upstream from Mars. *Journal of Geophysical Research: Space Physics*, *125*(9), e2020JA028221. https://doi.org/10.1029/2020JA028221

Halekas, J. S., Taylor, E. R., Dalton, G., Johnson, G., Curtis, D. W., McFadden, J. P., et al. (2015). The solar wind ion analyzer for MAVEN. *Space Science Reviews*, *195*(1–4), 125–151. https://doi.org/10.1007/s11214-013-0029-z

Heavens, N. G., Kleinböhl, A., Chaffin, M. S., Halekas, J. S., Kass, D. M., Hayne, P. O., et al. (2018). Hydrogen escape from Mars enhanced by deep convection in dust storms. *Nature Astronomy*, *2*(2), 126–132. https://doi.org/10.1038/s41550-017-0353-4

Jakosky, B. M., Lin, R. P., Grebowsky, J. M., Luhmann, J. G., Mitchell, D. F., Beutelschies, G., et al. (2015). The mars atmosphere and volatile evolution (MAVEN) mission. *Space Science Reviews*, *195*(1–4), 3–48. https://doi.org/10.1007/s11214-015-0139-x

Lee, M. A. (1989). Ultralow frequency waves at comets. In B. T. Tsurutani, & H. Oya (Eds.), Plasma waves and instabilities at comets and in magnetospheres (53, pp. 13–29). Washington, DC: American Geophysical Union (AGU). https://doi.org/10.1029/GM053p0013

Liu, D., Yao, Z., Wei, Y., Rong, Z., Shan, L., Arnaud, S., et al. (2020). Upstream proton cyclotron waves: occurrence and amplitude dependence on IMF cone angle at Mars from MAVEN observations. *Earth and Planetary Physics*, *4*(1), 51–61. https://doi.org/10.26464/epp2020002

Maltagliati, L., Montmessin, F., Fedorova, A., Korablev, O., Forget, F., & Bertaux, J.-L. (2011). Evidence of water vapor in excess of saturation in the atmosphere of Mars. *Science*, *333*(6051), 1868–1871. https://doi.org/10.1126/science.1207957

Maltagliati, L., Montmessin, F., Korablev, O., Fedorova, A., Forget, F., Mttnen, A., et al. (2013). Annual survey of water vapor vertical distribution and water aerosol coupling in the martian atmosphere observed by SPICAM/MEx solar occultations. *Icarus*, *223*(2), 942–962. https://doi.org/10.1016/j.icarus.2012.12.012

Mazelle, C., Le Quéau, D., & Meziane, K. (2000). Nonlinear wave-particle interaction upstream from the Earth's bow shock. *Nonlinear Processes in Geophysics*, *7*(3/4), 185–190. https://doi.org/10.5194/npg-7-185-2000

Mazelle, C., Meziane, K., LeQuau, D., Wilber, M., Eastwood, J. P., Rme, H., et al. (2003). Production of gyrating ions from nonlinear wave-particle interaction upstream from the Earth's bow shock: A case study from cluster-cis. *Planetary and Space Science*, *51*(12), 785–795. https://doi.org/10.1016/j.pss.2003.05.002

Mazelle, C., Meziane, K., Mitchell, D. L., Garnier, P., Espley, J. R., Hamza, A. M., et al. (2018). Evidence for neutrals-foreshock electrons impact at Mars. *Geophysical Research Letters*, *45*(9), 3768–3774. https://doi.org/10.1002/2018GL077298

Mazelle, C., & Neubauer, F. M. (1993). Discrete wave packets at the proton cyclotron frequency at comet P/Halley. *Geophysical Research Letters*, *20*(2), 153–156. https://doi.org/10.1029/92GL02613

Mazelle, C., Winterhalter, D., Sauer, K., Trotignon, J. G., Acuna, M. H., Baumgärtel, K., et al. (2004). Bow shock and upstream phenomena at Mars. *Space Science Reviews*, *111*, 115–181. https://doi.org/10.1023/B:SPAC.0000032717.98679.d0

Meziane, K., Mazelle, C. X., Romanelli, N., Mitchell, D. L., Espley, J. R., Connerney, J. E. P., et al. (2017). Martian electron foreshock from MAVEN observations. *Journal of Geophysical Research: Space Physics*, *122*(2), 1531–1541. https://doi.org/10.1002/2016JA023282

Modolo, R., Chanteur, G. M., Dubinin, E., & Matthews, A. P. (2005). Influence of the solar euv flux on the martian plasma environment. *Annales Geophysicae*, *23*(2), 433–444. https://doi.org/10.5194/angeo-23-433-2005

Rahmati, A., Larson, D. E., Cravens, T. E., Lillis, R. J., Halekas, J. S., McFadden, J. P., et al. (2017). Maven measured oxygen and hydrogen pickup ions: Probing the martian exosphere and neutral escape. *Journal of Geophysical Research: Space Physics*, *122*(3), 3689–3706. https://doi.org/10.1002/2016JA023371

Rahmati, A., Larson, D. E., Cravens, T. E., Lillis, R. J., Halekas, J. S., McFadden, J. P., et al. (2018). Seasonal variability of neutral escape from mars as derived from maven pickup ion observations. *Journal of Geophysical Research: Planets*, *123*(5), 1192–1202. https://doi.org/10.1029/2018JE005560

Romanelli, N., Bertucci, C., Gomez, D., Mazelle, C., & Delva, M. (2013). Proton cyclotron waves upstream from Mars: Observations from Mars global surveyor. *Planetary and Space Science*, *76*, 1–9. https://doi.org/10.1016/j.pss.2012.10.011

Romanelli, N., Mazelle, C., Chaufray, J.-Y., Meziane, K., Shan, L., Ruhunusiri, S., et al. (2016). Proton cyclotron waves occurrence rate upstream from Mars observed by MAVEN: Associated variability of the Martian upper atmosphere. *Journal of Geophysical Research: Space Physics*, *121*(11), 11113–11128. https://doi.org/10.1002/2016JA023270

Romanelli, N., Mazelle, C., & Meziane, K. (2018). Nonlinear wave-particle interaction: Implications for newborn planetary and backstreaming proton velocity distribution functions. *Journal of Geophysical Research: Space Physics*, *123*(2), 1100–1117. https://doi.org/10.1002/2017JA024691

Ruhunusiri, S., Halekas, J. S., Connerney, J. E. P., Espley, J. R., McFadden, J. P., Larson, D. E., et al. (2015). Low-frequency waves in the Martian magnetosphere and their response to upstream solar wind driving conditions. *Geophysical Research Letters*, *42*(21), 8917–8924. https://doi.org/10.1002/2015GL064968

Ruhunusiri, S., Halekas, J. S., Connerney, J. E. P., Espley, J. R., McFadden, J. P., Mazelle, C., et al. (2016). MAVEN observation of an obliquely propagating low-frequency wave upstream of Mars. *Journal of Geophysical Research: Space Physics*, *121*(3), 2374–2389. https://doi.org/10.1002/2015JA022306

Russell, C. T., Luhmann, J. G., Schwingenschuh, K., Riedler, W., & Yeroshenko, Y. (1990). Upstream waves at Mars: Phobos observations. *Geophysical Research Letters*, *17*(6), 897–900. https://doi.org/10.1029/GL017i006p00897

Sánchez-Lavega, A., del Río-Gaztelurrutia, T., Hernández-Bernal, J., & Delcroix, M. (2019). The onset and growth of the 2018 Martian Global Dust Storm. *Geophysical Research Letters*, *46*(11), 6101–6108. https://doi.org/10.1029/2019GL083207

Smith, M. D. (2009). Themis observations of Mars aerosol optical depth from 2002–2008. *Icarus*, *202*(2), 444–452. https://doi.org/10.1016/j.icarus.2009.03.027

Smith, M. D., & Guzewich, S. D. (2019). The Mars global dust storm of 2018. *49th International conference on environmental systems*. Boston, MA. Retrieved from https://ntrs.nasa.gov/citations/20190027303

Song, P., & Russell, C. T. (1999). Time series data analyses in space physics. *Space Science Reviews*, *87*(3–4), 387–463. https://doi.org/10.1023/A:1005035800454

Sonnerup, B. U. O., & Scheible, M. (1998). Minimum and maximum variance analysis. *Analysis methods for multi-spacecraft data*, *1*, 185–220.

Thiemann, E. M. B., Chamberlin, P. C., Eparvier, F. G., Templeman, B., Woods, T. N., Bougher, S. W., et al. (2017). The MAVEN EUVM model of solar spectral irradiance variability at Mars: Algorithms and results. *Journal of Geophysical Research: Space Physics*, *122*(3), 2748–2767. https://doi.org/10.1002/2016JA023512

Tsurutani, B. T. (1991). Comets: A laboratory for plasma waves and instabilities. In A. Johnstone (Ed.), Cometary plasma processes (Vol. 61, pp. 189–209). Washington, DC: American Geophysical Union (AGU). https://doi.org/10.1029/GM061p0189

Wei, H. Y., Cowee, M. M., Russell, C. T., & Leinweber, H. K. (2014). Ion cyclotron waves at Mars: Occurrence and wave properties. *Journal of Geophysical Research: Space Physics*, *119*(7), 5244–5258. https://doi.org/10.1002/2014JA020067

Wei, H. Y., & Russell, C. T. (2006). Proton cyclotron waves at Mars: Exosphere structure and evidence for a fast neutral disk. *Geophysical Research Letters*, *33*(23), L23103. https://doi.org/10.1029/2006GL026244

Wei, H. Y., Russell, C. T., Zhang, T. L., & Blanco-Cano, X. (2011). Comparative study of ion cyclotron waves at Mars, Venus and Earth. *Planetary and Space Science*, *59*(10), 1039–1047. https://doi.org/10.1016/j.pss.2010.01.004

Wu, C. S., & Davidson, R. C. (1972). Electromagnetic instabilities produced by neutral-particle ionization in interplanetary space. *Journal of Geophysical Research*, *77*(28), 5399–5406. https://doi.org/10.1029/JA077i028p05399

Wu, C. S., & Hartle, R. E. (1974). Further remarks on plasma instabilities produced by ions born in the solar wind. *Journal of Geophysical Research*, *79*(1), 283–285. https://doi.org/10.1029/JA079i001p00283

Yamauchi, M., Hara, T., Lundin, R., Dubinin, E., Fedorov, A., Sauvaud, J.-A., et al. (2015). Seasonal variation of Martian pick-up ions: Evidence of breathing exosphere. *Planetary and Space Science*, *119*, 54–61. https://doi.org/10.1016/j.pss.2015.09.013

Zhang, T. L., Delva, M., Baumjohann, W., Volwerk, M., Russell, C. T., Barabash, S., et al. (2008). Initial Venus express magnetic field observations of the Venus bow shock location at solar minimum. *Planetary and Space Science*, *56*(6), 785–789. https://doi.org/10.1016/j.pss.2007.09.012

Zhang, M. H. G., Luhmann, J. G., Nagy, A. F., Spreiter, J. R., & Stahara, S. S. (1993). Oxygen ionization rates at Mars and Venus: Relative contributions of impact ionization and charge exchange. *Journal of Geophysical Research*, *98*(E2), 3311–3318. https://doi.org/10.1029/92JE02229